

## MSA-3D: dissecting galaxies at $z \sim 1$ with high spatial and spectral resolution

IVANA BARIŠIĆ,<sup>1</sup> TUCKER JONES,<sup>1</sup> KRIS MORTENSEN,<sup>1</sup> THEMIYA NANAYAKKARA,<sup>2</sup> YUGUANG CHEN,<sup>1</sup> RYAN SANDERS,<sup>3,1</sup>  
JAMES S. BULLOCK,<sup>4</sup> KEVIN BUNDY,<sup>5</sup> CLAUDE-ANDRÉ FAUCHER-GIGUÈRE,<sup>6</sup> KARL GLAZEBROOK,<sup>2</sup> ALAINA HENRY,<sup>7,8</sup>  
MENGTING JU,<sup>9</sup> MATTHEW MALKAN,<sup>10</sup> TAKAHIRO MORISHITA,<sup>11</sup> DANAIL OBRESCHKOW,<sup>12,13</sup> NAMRATA ROY,<sup>14</sup>  
JUAN M. ESPEJO SALCEDO,<sup>15</sup> ALICE E. SHAPLEY,<sup>10</sup> TOMMASO TREU,<sup>10</sup> XIN WANG,<sup>9,16,17</sup> AND KYLE B. WESTFALL<sup>18</sup>

<sup>1</sup>*Department of Physics and Astronomy, University of California, Davis, 1 Shields Avenue, Davis, CA 95616, USA*

<sup>2</sup>*Centre for Astrophysics and Supercomputing, Swinburne University of Technology, Hawthorn, VIC 3122, Australia*

<sup>3</sup>*Department of Physics and Astronomy, University of Kentucky, 505 Rose Street, Lexington, KY 40506, USA*

<sup>4</sup>*Department of Physics and Astronomy, University of California Irvine, Irvine, CA 92697, USA*

<sup>5</sup>*Department of Astronomy & Astrophysics, University of California, Santa Cruz, 1156 High St, CA 95064, USA*

<sup>6</sup>*Department of Physics & Astronomy and CIERA, Northwestern University, 1800 Sherman Ave, Evanston, IL 60201, USA*

<sup>7</sup>*Space Telescope Science Institute, 3700 San Martin Drive, Baltimore, MD 21218, USA*

<sup>8</sup>*Department of Physics and Astronomy, Johns Hopkins University, Baltimore, MD 21218, USA*

<sup>9</sup>*School of Astronomy and Space Science, University of Chinese Academy of Sciences (UCAS), Beijing 100049, China*

<sup>10</sup>*Department of Physics and Astronomy, University of California Los Angeles, 430 Portola Plaza, Los Angeles, CA 90095, USA*

<sup>11</sup>*IPAC, California Institute of Technology, MC 314-6, 1200 E. California Boulevard, Pasadena, CA 91125, USA*

<sup>12</sup>*International Centre for Radio Astronomy Research (ICRAR), M468, University of Western Australia, Perth, WA 6009, Australia*

<sup>13</sup>*Australian Research Council, ARC Centre of Excellence for All Sky Astrophysics in 3 Dimensions (ASTRO 3D), Australia*

<sup>14</sup>*Center for Astrophysical Sciences, Department of Physics and Astronomy, Johns Hopkins University, Baltimore, MD 21218, USA*

<sup>15</sup>*Max-Planck-Institut für extraterrestrische Physik (MPE), Giessenbachstr., 85748 Garching, Germany*

<sup>16</sup>*National Astronomical Observatories, Chinese Academy of Sciences, Beijing 100101, China*

<sup>17</sup>*Institute for Frontiers in Astronomy and Astrophysics, Beijing Normal University, Beijing 102206, China*

<sup>18</sup>*University of California Observatories, University of California, Santa Cruz, 1156 High St., Santa Cruz, CA 95064, USA*

### ABSTRACT

Integral field spectroscopy (IFS) is a powerful tool for understanding the formation of galaxies across cosmic history. We present the observing strategy and first results of MSA-3D, a novel JWST program using multi-object spectroscopy in a slit-stepping strategy to produce IFS data cubes. The program observed 43 normal star-forming galaxies at redshifts  $0.5 \lesssim z \lesssim 1.5$ , corresponding to the epoch when spiral thin-disk galaxies of the modern Hubble sequence are thought to emerge, obtaining kpc-scale maps of rest-frame optical nebular emission lines with spectral resolution  $R \simeq 2700$ . Here we describe the multiplexed slit-stepping method which is  $> 15$  times more efficient than the NIRSpect IFS mode for our program. As an example of the data quality, we present a case study of an individual galaxy at  $z = 1.104$  (stellar mass  $M_* = 10^{10.3} M_\odot$ , star formation rate =  $3 M_\odot \text{ yr}^{-1}$ ) with prominent face-on spiral structure. We show that the galaxy exhibits a rotationally supported disk with moderate velocity dispersion ( $\sigma = 36_{-4}^{+5} \text{ km s}^{-1}$ ), a negative radial metallicity gradient ( $-0.020 \pm 0.002 \text{ dex kpc}^{-1}$ ), a dust attenuation gradient, and an exponential star formation rate density profile which closely matches the stellar continuum. These properties are characteristic of local spirals, indicating that mature galaxies are in place at  $z \sim 1$ . We also describe the customized data reduction and original cube-building software pipelines which we have developed to exploit the powerful slit-stepping technique. Our results demonstrate the ability of JWST slit-stepping to study galaxy populations at intermediate to high redshifts, with data quality similar to current surveys of the  $z \sim 0.1$  universe.

*Keywords:* Galaxy formation (595), Galaxy evolution (594), Disk galaxies (391), High-redshift galaxies (734), Astronomical techniques (1684)

## 1. INTRODUCTION

Galaxies in the nearby universe can be classified according to the “Hubble sequence” of star-forming disks with spiral arms, and passive spheroids (e.g., Hubble 1926; Kennicutt 1998). A similar sequence persists at cosmological redshifts of at least  $z \gtrsim 3$  (e.g., Wuyts et al. 2011; Mortlock et al. 2013; Zhang et al. 2019; Straatman et al. 2016). Integral field spectroscopy (IFS) has proven critical in understanding the structure of disk galaxies in the early universe, in particular by observing strong emission lines such as H $\alpha$  and CO transitions (e.g., see reviews by Glazebrook 2013; Förster Schreiber & Wuyts 2020). IFS surveys have revealed that disk galaxies at  $z \gtrsim 2$  are characterized by higher velocity dispersion  $\sigma$  (and lower ratio of rotation to dispersion support,  $V/\sigma$ ; e.g., Übler et al. 2019; Leethochawalit et al. 2016; Simons et al. 2016; Epinat et al. 2012; Jones et al. 2021), scale heights characteristic of thick disks (e.g., Elmegreen & Elmegreen 2006; Hamilton-Campos et al. 2023), shallower gas-phase metallicity gradients (indicating radial mixing; e.g., Wang et al. 2019; Wang et al. 2020), and clumpier star formation morphology (Förster Schreiber et al. 2011; Guo et al. 2015; Livermore et al. 2015), typically lacking the spiral structure seen at low redshifts.

Different factors contributing to the higher gas velocity dispersions at higher redshifts have been proposed theoretically. One effect is that higher gas accretion rates result in higher gas fractions in galaxies, which in equilibrium disk models correlate with higher velocity dispersions (e.g., Dekel et al. 2009; Faucher-Giguère et al. 2013; Brennan et al. 2017; Pillepich et al. 2019; Forbes et al. 2023). Recently, high-resolution cosmological simulations have also found that the thermodynamic state of the circumgalactic medium (CGM) correlates tightly with the emergence of thin disks that can support spiral structure. In particular, Hafen et al. (2022) showed that a virialized inner CGM allows the gas to accrete with coherent angular momentum onto central galaxies via hot-mode accretion, which promotes the formation of thin disks. Stern et al. (2021) also argued that the high and near-uniform thermal pressure in a virialized inner CGM helps confine star formation-driven outflows. In a related study, Hopkins et al. (2023) emphasized the role of the concentration and depth of the gravitational potential. The former is a determinant of whether there is a well-defined dynamical center around which rotation can stabilize, while the latter (which correlates with CGM virialization) contributes to the confinement of outflows via gravity (see Byrne et al. 2023, for a discussion of outflow confinement by hot gas pres-

sure vs. gravity). In this picture in which the emergence of thin disks is connected to the virialization of the inner CGM and the depth of the gravitational potential, mass rather than redshift is a primary predictor of thin-disk formation. In practice, this leads to an increased thin-disk fraction going to lower redshift because the abundance of sufficiently massive halos ( $M_{\text{halo}} \gtrsim \text{a few} \times 10^{11} M_{\odot}$ ) increases with decreasing redshift.

Observationally, the epoch around  $z \simeq 1$  is thought to be a time of “disk settling” during which thin spiral disks become prominent among star forming galaxies (e.g. Kassin et al. 2012; Miller et al. 2011, 2012; Simons et al. 2017).

Surveys of galaxy kinematics indicate a rise in the degree of rotational support revealed by increasing  $V/\sigma$  toward lower redshifts (as well as higher  $V/\sigma$  at higher masses; e.g., Wisnioski et al. 2019; Simons et al. 2016; Tiley et al. 2021). For example, Simons et al. (2017) show that the fraction of massive galaxies (stellar mass  $M_* > 10^{9.5} M_{\odot}$ ) with  $V/\sigma > 3$  increases from  $\sim 20\%$  at  $z = 2$  to approximately 50% at  $z = 1$ . Morphological studies similarly show an increasing fraction of disk and spiral galaxies at lower redshifts. While clear examples of spiral galaxies have been found as early as  $z \gtrsim 3$  (e.g., Wu et al. 2023), they are rare at such redshifts. Recent analysis of James Webb Space Telescope (JWST) imaging by Kuhn et al. (2024) found that the fraction of massive galaxies ( $M_* > 10^{10} M_{\odot}$ ) with visually identifiable spiral structure increases from  $\sim 15\%$  at  $z = 2$  to 43% at  $z = 1$ , although the true spiral fraction is likely higher given the challenge of detecting spiral structure at high redshifts. Previous investigations of Hubble Space Telescope images found broadly similar results (e.g., Margalef-Bentabol et al. 2022). Overall, morphological and kinematic properties both indicate that well-ordered disks are more common at lower redshift, with the population of moderately massive star-forming galaxies becoming dominated by spiral disk morphologies at around  $z \simeq 1$ .

High-quality IFS observations of strong nebular emission lines (such as H $\alpha$ , [N II], and [O III]) can provide a comprehensive view of individual high-redshift galaxies and their evolutionary pathways. For example, kpc-scale kinematic measurements can reveal the mass density profile and dark matter fraction (e.g., Genzel et al. 2020). In addition to kinematics and morphology, strong emission line ratios provide information about ionization sources (e.g., Wright et al. 2010; Belli et al. 2017) and gas-phase metallicity (e.g., Maiolino & Mannucci 2019). Radial metallicity gradients have emerged as a valuable probe of the “baryon cycle” of gas accretion and feedback-driven outflows which regulate galaxy for-

mation (Tumlinson et al. 2017; Faucher-Giguère & Oh 2023), as established by various theoretical investigations (Gibson et al. 2013; Ma et al. 2017; Hemler et al. 2021). Metallicity and kinematic maps can also identify signatures of metal-poor gas accretion (e.g., Sánchez Almeida et al. 2015; Ju et al. 2022). Observations of high-redshift galaxies have found a large scatter in gradient slopes, which are shallower on average than in nearby spiral galaxies and show substantial azimuthal variation (e.g., Wang et al. 2017, 2020, 2022; Curti et al. 2020). As with kinematics, spatial resolution of  $\lesssim 1$  kpc is essential for accurate results (Yuan et al. 2013; Jones et al. 2013). IFS emission line maps can thus not only identify disks via their kinematic signatures, but also probe the properties such as accretion and gravitational potential, which allow the formation of thin spiral disks.

A key challenge for high redshift galaxies is to obtain IFS with sufficient angular resolution, as well as spectral resolution and signal-to-noise ratio. For the rest-frame optical emission lines, the vast majority of current samples are observed with seeing-limited data of  $\sim 0''.5$ – $1''.0$  resolution. This corresponds to  $\sim 4$ – $8$  kpc at  $z \gtrsim 1$  (e.g., Förster Schreiber et al. 2009; Wisnioski et al. 2015, 2019; Stott et al. 2016) which is comparable to massive galaxy sizes at these redshifts. Such data cannot clearly distinguish disks from merging systems at moderate to high redshifts (e.g., Leethochawalit et al. 2016; Simons et al. 2019). Instead, the prevalence and kpc-scale structure of rotationally supported disks at redshifts  $z \gtrsim 2$  has been established in smaller samples with adaptive optics (AO) assisted observations (e.g., Genzel et al. 2006, 2008; Förster Schreiber et al. 2018; Espejo Salcedo et al. 2022), including AO surveys of gravitationally lensed galaxies which can probe  $\sim 100$  parsec scales (Stark et al. 2008; Jones et al. 2010; Leethochawalit et al. 2016; Hirsten et al. 2019). However, current AO systems are most effective only at wavelengths  $\gtrsim 1.5 \mu\text{m}$ . Consequently, most AO IFS samples are limited to  $z \gtrsim 1.5$  where H $\alpha$  and other strong lines can be observed with high Strehl ratios. As a result, the epoch of spiral disk emergence at  $z \simeq 0.5$ – $1.5$  has not been explored with suitable resolution. Additionally, ground-based observations suffer from a time-variable atmosphere and point-spread function (PSF), which is especially complex for AO data. This leads to challenges in recovering properties such as galaxy velocity dispersions and  $V/\sigma$  (e.g., Davies et al. 2011; Burkert et al. 2016). We note that space-based grism observations are able to obtain kpc-scale spatial resolution but are limited by poor spectral resolution ( $R \lesssim 300$ ; e.g., Simons et al. 2021; Wang et al. 2020; Jones et al. 2015b), while ground-based IFS sur-

veys are limited to coarse spatial resolution at the key wavelengths.

JWST’s unique capabilities now enable excellent spatial *and* spectral resolution, combined with good sensitivity at the relevant wavelengths for mapping rest-frame optical emission lines at  $z \gtrsim 0.5$  with the NIRSpec instrument (Jakobsen et al. 2022; Böker et al. 2023). Importantly, JWST delivers reliable results via a stable PSF with high Strehl, in contrast to ground-based AO observations. However, NIRSpec’s integral field unit (IFU) is effectively limited to single-object observations given the  $3''$  field of view. Building sufficient samples to characterize the galaxy population at high redshifts is thus a time-intensive prospect. To efficiently obtain high-quality data for large samples, we have instead turned to NIRSpec’s Micro-Shutter Assembly (MSA) which provides multiplexed observations with  $0''.2$  wide slitlets. By utilizing a “slit-stepping” observing sequence (e.g., Ho et al. 2017; Genzel et al. 2013), we are able to obtain IFS data for  $>40$  galaxies simultaneously in  $< 10\%$  of the time that would be required for an equivalent IFU survey. This paper describes our first application and example results of this novel multiplexed slit-stepping method via the program JWST-GO-2136, in which we observed 43 galaxies at  $0.5 < z < 1.7$ , corresponding to the disk settling epoch when spiral structure becomes prominent. As we are obtaining 3-D data cubes using NIRSpec’s MSA strategy, we dub our program MSA-3D<sup>1</sup>.

In this paper, we demonstrate that our technique provides excellent data quality for mapping  $z \sim 1$  galaxies, which our team is analyzing with a series of planned papers on their kinematics, metallicity gradients, excitation sources, star formation morphology, and more. Notably, our sample size obtained with a  $\simeq 30$  hour MSA slit-stepping program is comparable to the 47 galaxies targeted by the 273-hour NIRSpec guaranteed time GA-NIFS program using the IFU (Perna 2023). Given the large efficiency gain over JWST’s IFU mode, our method represents the most pragmatic opportunity to build large samples (tens to hundreds) of kpc-resolution IFS data of distant galaxies to study their evolution across cosmic time. Accordingly, one of our objectives in this paper is to simply demonstrate the effectiveness of this observing strategy. We urge its adoption for large multiplexed galaxy surveys with JWST.

This paper describes the observational strategy and data reduction procedure, serving as a reference for the MSA-3D program and subsequent papers. We also de-

<sup>1</sup> With a nod to previous surveys 3D-HST (Brammer et al. 2012) and KMOS<sup>3D</sup> (Wisnioski et al. 2015).

scribe a case study of an individual galaxy illustrating the variety of analyses enabled by MSA-3D. Various analyses of the broader sample are in preparation or planned. These include a companion paper by Ju et al. (in prep.) presenting the gas-phase metallicity gradients, a study of the gas ionization mechanisms and active galactic nuclei (Roy et al. in prep.), and other topics such as kinematics, angular momentum, dark matter content, and star formation rate profiles. The structure of the present paper is as follows. In Section 2 we describe the JWST observations, including the sample selection, motivation and implementation of the slit-stepping methodology, and data processing. Section 3 presents a case study of a  $z = 1.104$  spiral galaxy based on emission line measurements from our data. We describe its kinematic structure, gas-phase metallicity and radial gradient, dust attenuation and radial gradient, and overall disk structure as traced by the surface brightness profile. In Section 4 we discuss our results, and future analyses enabled by the MSA-3D program, in the context of broad efforts to understand the growth and evolution of galaxies across cosmic history. Throughout this work we adopt a flat  $\Lambda$ CDM cosmology with  $H_0 = 69.6 \text{ km s}^{-1} \text{ Mpc}^{-1}$  and  $\Omega_M = 0.286$  (Bennett et al. 2014).

## 2. OBSERVATIONS AND DATA PROCESSING

This paper is based on spectroscopic data from the JWST Cycle 1 program GO-2136 (PI: Jones). This program obtained NIRSpec Micro-Shutter Assembly (MSA) observations of 43 galaxies at  $z \sim 1$ , using a slit-stepping strategy to provide spatially resolved kpc-scale pseudo-integral field spectroscopy. Data were taken on 2023 March 29-30. We used the G140H/F100LP grating/filter combination, covering wavelengths 0.97–1.82  $\mu\text{m}$  with full-width at half maximum (FWHM) spectral resolution  $\Delta\lambda \simeq 5.2 \text{ \AA}$  corresponding to  $R \simeq 2700$  resolving power. As described below, dithered exposures cover a contiguous  $1''.8 \times (2''.0\text{--}3''.0)$  field of view for each target galaxy, depending on the number of slitlets used. The observations are optimized to map strong rest-frame optical emission lines in galaxies spanning the epoch in which modern thin disks emerge (e.g. Kassin et al. 2012; Miller et al. 2012; Simons et al. 2017; Wisnioski et al. 2019). In this section, we describe the observing strategy, the merits of the MSA slit-stepping approach relative to the IFU mode, and the data reduction steps performed to produce data cubes.

### 2.1. Sample selection

Our target field is the Extended Groth Strip (EGS), a well-studied extragalactic field with extensive photometric and spectroscopic survey data including from the

CANDELS (Koekemoer et al. 2011), 3D-HST (Momcheva et al. 2016), CEERS (Finkelstein et al. 2023), DEEP2 and DEEP3 (Newman et al. 2013), and MOSDEF (Kriek et al. 2015) surveys. This field was selected in part to overlap with the CEERS JWST Early Release Science imaging area. Our program science goals require mapping multiple nebular emission lines to study resolved kinematics, star formation rates, metallicity, and ionization mechanisms. Our primary sample selection is to target  $\text{H}\alpha$ ,  $[\text{N II}]$ ,  $[\text{S II}]$ ,  $[\text{O III}]$ , and  $\text{H}\beta$ . These lines are accessible from  $z = 1.0\text{--}1.7$  using the G140H/F100LP grating/filter. We adopt a secondary target redshift range  $z = 0.5\text{--}1.0$  which includes coverage of  $\text{H}\alpha$ ,  $[\text{N II}]$ ,  $[\text{S II}]$ ,  $[\text{S III}]$ , and  $\text{H I}$  Paschen lines, enabling similar measurements. For target selection, we required spectroscopic redshift confirmation and multi-wavelength HST photometry from the CANDELS survey (Koekemoer et al. 2011), which, along with other imaging data, ensures reliable spectral energy distribution fitting based measurements of stellar mass and star formation rate (SFR). For selection purposes, we adopted stellar population parameter values from the 3D-HST survey catalogue (Skelton et al. 2014; Momcheva et al. 2016). In total, we identified a parent catalog of 1336 galaxies in the target redshift range  $0.5 < z < 1.7$ , and further restricted the MSA target selection to the 72% of these galaxies with secure spectroscopic redshifts. The sample is shown in the left panel of Figure 1.

In building our spectroscopic sample, we applied selection criteria of stellar mass  $M_* > 10^9 M_\odot$  and  $\text{SFR} > 0.6 M_\odot \text{ yr}^{-1}$ . This ensures the observed targets probe the star forming main sequence at  $z \sim 1$  (e.g., Whitaker et al. 2012; Speagle et al. 2014) and have suitably bright and spatially extended nebular emission. However, we did not impose any selection criteria based on galaxy size or surface brightness to avoid biases in the observed sample. In designing the MSA mask, we also targeted regions with JWST/NIRCam coverage from the CEERS program. Ultimately, the MSA mask includes 43 target galaxies, of which 19 are within the current NIRCam footprint. Table 1 lists properties and emission line coverage of these 43 galaxies, of which 32 are at  $z > 1$  and 11 are at  $0.5 < z < 1$ . Coverage of the  $\text{H}\alpha$  line is present in 38 of the 43 galaxies (88%), whereas in the remainder of the sample it falls in the chip gap or off the detectors. In this paper we present a case study analysis of galaxy ID 8512 at  $z = 1.104$  with  $M_* = 10^{10.32} M_\odot$  and  $\text{SFR} = 3.2 M_\odot \text{ yr}^{-1}$ . We selected this target for initial analysis based on its clear spiral disk morphology. It is otherwise representative of the more massive galaxies in the observed sample.

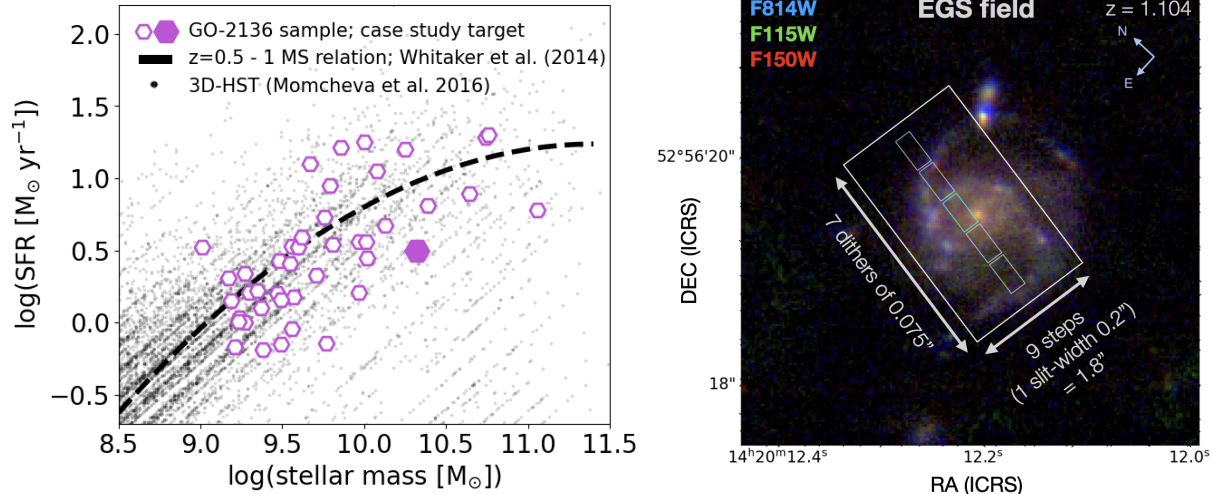


**Figure 1:** *Left:* The MSA-3D target sample from program JWST-GO-2136 (purple hexagons) is selected to represent typical star-forming galaxies within the redshift range  $z = 0.5\text{--}1.7$ . We show their star formation rates and stellar masses, along with the full 3D-HST sample within the same redshift range. The black dashed line depicts the star forming main sequence relation from Whitaker et al. (2014). Our targets are representative of the star-forming population at stellar masses  $\gtrsim 10^9 M_\odot$ . *Right:* Color image of the  $z = 1.1$  galaxy analyzed in this paper (ID 8512; blue: HST/ACS F814W, green: JWST/NIRCam F115W, red: JWST/NIRCam F150W). The galaxy shows a clear face-on spiral morphology. This target was observed with five NIRSpec/MSA slitlets, shown as small grey rectangles. Arrows show the slit-stepping approach with 9 steps of  $0''.2$  in the dispersion direction, and 7 dithers of  $0''.075$  in the cross dispersion direction. Cross-dispersion steps are used to remove the bar shadows ( $0''.075$  width) which can be seen as the gaps between slitlets. The larger rectangle shows the full  $1''.8 \times 3''.0$  sky area of the resulting IFS data cube, of which each pixel in the central  $1''.8 \times 2''.1$  has uniform coverage of 117 minutes from six exposures on-source (and a seventh exposure affected by bar shadows).

## 2.2. Slit-stepping observing strategy

A key unique aspect of these JWST Cycle 1 observations is the slit-stepping strategy illustrated in Figure 2. We observed the same MSA mask configuration in a grid of 63 different pointings: 9 steps along the dispersion direction at a width of a slitlet ( $0''.2$ ), with 7 dithers along the cross-dispersion direction stepped by the width of a barshadow ( $0''.075$ ). A single exposure of 19.5 minutes was taken at each of the 63 dithered positions, using the NRSIRS2 readout mode with 16 groups. This  $9 \times 7$  dither pattern provides nearly uniform depth, where each sky position is observed with six exposures on-source (117 minutes) and one exposure affected by a bar shadow. Each target galaxy is covered with a minimum of 3 slitlets of  $\sim 0''.5$  length each. We add up to 2 additional slitlets wherever possible, avoiding MSA slit collisions. This results in data cubes spanning  $1''.8 \times (2''.0\text{--}3''.0)$  depending on the number of slitlets (3–5), as illustrated in Figures 1 and 2. The region with uniform full exposure coverage is  $1''.8 \times (1''.1\text{--}2''.1)$ , corresponding to approximately  $15 \times (10\text{--}18)$  kpc at our target redshifts. We emphasize that the slit-stepping strategy is designed for *contiguous uniform depth* in this field of

view. In contrast, a rectangular grid of slitlets (e.g.,  $9 \times 5$ ) on the MSA has only  $\sim 65\%$  illumination with approximately one-third of the area obscured by bar shadows. Our observations effectively remove these bar shadows to provide contiguous sky coverage Figure 2).

The areal coverage set by the number of slit-steps (9) and slitlets per target ( $\geq 3$ ) is chosen to sample galaxy radii  $\gtrsim 3R_s$ , where  $R_s \simeq 2.5$  kpc is the typical scale radius of star-forming galaxies at the upper mass range of our sample ( $M_* \sim 10^{11} M_\odot$ ). A key goal is to map galaxy kinematics beyond the “turnover radius” ( $R > 2.2R_s$ ) corresponding to the maximum circular velocity for an exponential disk (Freeman 1970). The depth of  $\sim 2$  hours effective exposure time is sufficient to reach  $\sim 5\sigma$  detections of  $H\alpha$  emission in an  $0''.1 \times 0''.2$  resolution element at  $R \simeq 3R_s$  for typical  $z \simeq 1$  galaxies across the targeted mass range, based on surface brightness profiles measured from HST grism spectroscopy (Nelson et al. 2016a). In addition, the total program time of  $\sim 29$  hours including overheads allowed all spectra to be taken in a single visit, to avoid positional uncertainty which may arise from multiple visits. The program is thus optimized to map  $H\alpha$  emission in

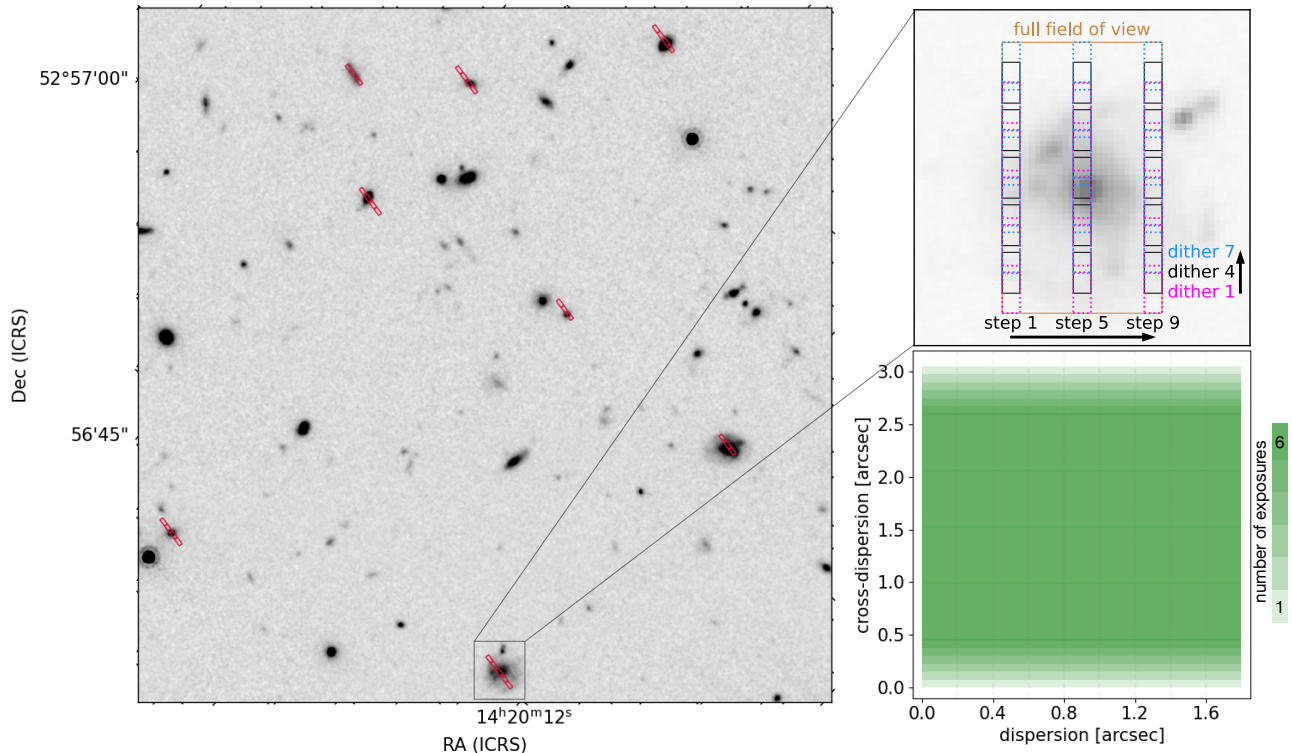


**Figure 2:** Illustration of IFS multiplexing achieved with MSA-3D’s slit-stepping strategy. *Left:* A portion of NIR-Spec/MSA’s field of view. Red slitlets show the central MSA pointing for  $z \sim 1$  galaxies targeted by this program, overlaid on a near-infrared HST F160W image. Each galaxy is targeted with between 3–5 slitlets. *Top right:* Fuchsia, black, and blue boxes show slitlet positions for a subset of 9 out of the 63 pointings overlaid on a JWST/NIRCam F444W image of an example target galaxy. These represent the first, middle, and final positions in both the dispersion direction (“steps”) and cross-dispersion direction (“dithers”). Collectively the 63 pointings provide contiguous coverage over the field of view. *Bottom right:* Green shading shows the effective number of exposures at each position within the field, ranging from one to six. Gray dashed vertical lines denote the  $0''.2$  slit width. Our strategy achieves nearly uniform six-exposure depth over the central region, effectively eliminating the MSA bar shadows. This observing strategy results in IFS data for all objects on the MSA mask.

$z \sim 1$  galaxies out to several disk scale radii, with simultaneous coverage of additional strong optical emission lines. This enables our scientific goals to map gas kinematics, metallicity, ionization mechanisms, dust attenuation, and star formation rate on kpc scales.

### 2.3. Comparison of slit-stepping vs. IFU modes

Here we briefly compare our slit-stepping strategy with the conventional integral field unit spectrograph mode of JWST/NIRSpec. The IFU is effectively limited to observing a single galaxy at a time given its  $3'' \times 3''$  field of view. The IFU is also less sensitive, requiring approximately  $4\times$  longer on-source integration than the MSA to reach the same sensitivity in a fixed aperture (e.g.,  $0''.1 \times 0''.2$ ). Thus the IFU would require  $\sim 8$  hours on-source per galaxy to reach the same depth as our MSA observations. In contrast we obtained spatially resolved spectroscopy for 43 galaxies with only  $\sim 20$  hours of exposure time, thanks to the MSA’s multiplexing ca-

pability. This represents a factor  $\sim 15\times$  advantage in exposure time alone; the total time advantage may be up to two times greater considering larger total slew time overheads to observe a sample of objects with the IFU mode.

The primary disadvantage of the MSA for this work is the  $0''.2$  slitlet width, which undersamples the PSF and is coarser than the IFU’s  $0''.1$  spaxels. The MSA nonetheless provides sufficient spatial sampling for our objectives. Another disadvantage of the MSA is that the spectral coverage varies depending on target position. This is a modest effect in our case: 12% of targets (5/43) do not have  $H\alpha$  coverage due to their location on the MSA mask. The spectral coverage effect is most severe with the high resolution gratings (including G140H used here); a program using medium or low resolution gratings would be less affected. Ultimately the most significant of the above effects are the MSA’s sensitivity

**Table 1:** Properties of the target sample. The ID numbers, stellar masses, and star formation rates are taken from the 3D-HST catalogs (Brammer et al. 2012; Skelton et al. 2014). For each object we list the strong nebular emission lines covered by the NIRSspec/MSA spectra. [N II], [S II], [O III], and [S III] refer to both lines in the doublet unless specified otherwise.

ID	RA	Dec	$z$	stellar mass $\log(M_*/M_\odot)$	SFR $M_\odot\text{yr}^{-1}$	emission lines
2111	215.0627824	52.9070766	0.58	9.97	1.6	H $\alpha$ , [N II], [S II], [S III]
2145	215.0694675	52.9108516	1.17	9.19	1.4	H $\alpha$ , [N II], [S II], H $\beta$ , [O III]
2465	215.0704381	52.9137241	1.25	9.30	1.6	H $\alpha$ , [N II], [S II], H $\beta$ , [O III]
2824	215.0685025	52.914333	0.98	9.49	0.7	H $\alpha$ , [N II], [S II], [O III], [S III] $\lambda$ 9069
3399	215.042511	52.8996031	1.34	9.81	3.5	H $\alpha$ , [N II], [S II], H $\beta$ , [O III]
4391	215.0676175	52.9232437	1.08	9.48	2.7	H $\alpha$ , [N II], H $\beta$ , [O III]
6199	215.0450158	52.9194652	1.59	10.00	17.8	H $\alpha$ , [N II], [S II], H $\beta$
6430	215.0131444	52.8980378	1.17	9.79	8.9	H $\alpha$ , [N II], [S II], H $\beta$ , [O III] $\lambda$ 4959
6848	215.0355588	52.9166925	1.57	10.64	7.8	H $\alpha$ , [N II], [S II], [O III]
7314	214.9989097	52.8925151	1.28	9.55	2.6	H $\alpha$ , [N II], H $\beta$ , [O III]
7561	215.0609094	52.9383828	1.03	9.21	0.7	H $\alpha$ , [N II], [S II], H $\beta$ , [O III], [S III] $\lambda$ 9069
8365	215.0599904	52.9422373	1.68	9.56	3.4	H $\alpha$ , [N II], [S II], H $\beta$ , [O III]
8512	215.0497806	52.9380795	1.10	10.32	3.2	H $\alpha$ , [N II], [S II], H $\beta$ , [O III]
8576	215.0595679	52.9434335	1.57	9.60	3.3	H $\alpha$ , [N II], [S II], H $\beta$ , [O III]
8942	215.0094032	52.9100655	1.18	9.86	16.2	H $\alpha$ , [N II], [S II], H $\beta$ , [O III] $\lambda$ 4959
9337	214.9957065	52.9019407	1.17	9.27	2.2	H $\alpha$ , [N II], [S II], H $\beta$ , [O III]
9424	214.9926533	52.900911	0.98	9.76	5.4	H $\alpha$ , [N II], [S II]
9482	215.0530158	52.9442406	1.21	9.77	0.7	H $\alpha$ , [N II][S II], H $\beta$ , [O III]
9527	215.0085005	52.9123786	1.42	10.02	2.8	H $\alpha$ , [N II], H $\beta$ , [O III]
9636	215.0365985	52.9328783	0.74	9.35	1.7	H $\alpha$ , [N II], [S II], [S III]
9812	215.0402843	52.9376004	0.74	9.97	3.6	H $\alpha$ , [N II], [S II], [S III]
9960	215.031894	52.9331513	1.51	11.06	6.0	H $\alpha$ , [N II], [S II]
10107	214.9817759	52.8975743	1.01	10.01	3.6	H $\alpha$ , [N II], [S II], [O III]
10502	214.9857711	52.9033048	1.23	10.13	4.7	H $\alpha$ , [N II], H $\beta$ , [O III]
10752	215.0403761	52.9413773	1.73	9.62	3.9	H $\beta$ , [O III]
10863	215.0551264	52.9529908	1.03	9.24	1.1	H $\alpha$ , [N II], H $\beta$ , [O III], [S III] $\lambda$ 9069
10910	215.0561932	52.9553701	0.74	9.57	1.5	H $\alpha$ , [N II], [S II], [S III]
11225	215.0415788	52.9454655	1.05	9.67	12.6	H $\alpha$ , [N II], [S II], H $\beta$ , [O III]
11539	214.9819651	52.9051336	1.61	10.39	6.5	H $\beta$ , [O III]
11702	214.9794086	52.9031601	1.23	9.37	1.3	H $\beta$ , [O III]
11843	215.0390468	52.9471037	1.46	10.74	19.0	H $\alpha$ , [N II], [S II], H $\beta$ , [O III]
11944	215.0369901	52.9453937	1.04	9.27	1.0	H $\alpha$ , [N II], [S II], H $\beta$ , [O III]
12015	215.0323151	52.9431798	1.24	10.08	11.2	H $\alpha$ , [N II], [S II], H $\beta$ , [O III]
12071	215.0219665	52.9360567	1.28	9.47	1.6	H $\alpha$ , [N II], [S II], H $\beta$ , [O III]
12239	215.0495343	52.9560252	0.89	9.49	1.5	H $\alpha$ , [N II], [S II], [S III]
12253	215.0442096	52.9520815	1.03	9.17	2.0	[S II], H $\beta$ , [O III]
12773	215.029765	52.9451588	0.95	9.23	1.0	H $\alpha$ , [N II], [S II]
13182	214.99983	52.9268186	1.54	10.25	15.8	H $\beta$ , [O III]
13416	215.0252815	52.9456859	1.54	10.76	20.0	H $\alpha$ , [N II], [S II], [O III]
18188	214.9839579	52.9413562	0.82	9.56	0.9	H $\alpha$ , [N II], [S II]
18586	214.9712282	52.9337862	0.76	9.01	3.3	H $\alpha$ , [N II], [S II]
19382	214.9765628	52.9414977	1.03	9.38	0.6	H $\alpha$ , [N II], [S II], [O III]
29470	214.9689505	52.9453733	1.04	9.71	2.1	H $\alpha$ , [N II], [S II], H $\beta$ , [O III]

and multiplexing advantages, which deliver an order of magnitude faster survey speed for building spatially resolved spectroscopic samples. In sum, MSA slit-stepping is strongly preferred for our scientific program due to large efficiency gains compared to the IFU mode.

In general, the slit-stepping mode is powerful for surveys making use of the MSA’s multiplexing capability, whereas the IFU mode is more effective for targets which are sparse on the sky. Here we roughly quantify the relative efficiency of the two modes for a general use case. Assuming that  $N_{mask}$  targets can be observed on a single MSA mask, with spatial coverage required over a diameter  $D$  (such that the number of slit-steps required is  $D/0''.2$ ), the efficiency gain in exposure time required for MSA slit-stepping compared to the IFU is

$$G = \frac{\text{IFU exposure time}}{\text{slit stepping exposure time}} \approx 3.5N_{mask} \left( \frac{0''.2}{D} \right). \quad (1)$$

The factor of  $\approx 3.5$  arises from the IFU’s lower sensitivity (contributing  $\sim 4\times$ ) multiplied by the fractional area covered by MSA slitlets ( $\sim 0.87 = 0''.46$  slitlet length out of  $0''.53$  pitch, with  $0''.075$  obscured by a bar shadow). Equation 1 is valid for  $D \leq 3''$  such that targets can be observed with a single IFU pointing. For more extended sources requiring  $N_{IFU}$  pointings per target, the result becomes

$$G \approx 3.5N_{mask} \left( \frac{0''.2}{D} \right) N_{IFU}. \quad (2)$$

A gain  $G > 1$  indicates the slit-stepping approach is more efficient. As an example, for cases requiring a  $3''.0$  diameter field of view, slit-stepping is more efficient when  $\gtrsim 5$  targets can be observed on an MSA mask. The IFU is more efficient ( $G < 1$ ) if targets are more sparse on the sky. The slit-stepping mode can also be more efficient for observing individual sources which are highly extended ( $D \gtrsim 10''$ , where  $N_{IFU}$  becomes large). We note that individual science cases may prefer the IFU for reasons such as spatial sampling or other complexities. Additionally some cases require a modest sample size  $N_{sample} < N_{mask}$ , such that  $N_{mask}$  should be replaced by  $N_{sample}$  for purposes of total efficiency. Otherwise, for use cases in which MSA spectra are suitable, Equations 1 and 2 offer approximate guidance on which mode is more appropriate in terms of survey speed.

#### 2.4. Reduction Pipeline and Data Cube Construction

As our slit-stepping observing methodology is non-standard, we have developed a custom data reduction procedure to process the raw data and ultimately construct data cubes for each target. We primarily use procedures from the JWST Science Calibration Pipeline developed by the Space Telescope Science Institute

(STScI) and augment this pipeline with custom steps to improve performance with the small sub-slitlet dithers. We use versions 1.9.6 (CRDS file “jwst\_1075.pmap”) and 1.10.2 (CRDS file “jwst\_1105.pmap”) of the standard reduction pipeline for stages 1 and (2, 3) respectively. We selected version 1.9.6 for Stage 1 to avoid the significant negative pixel artifacts that occurred with version 1.10.2. Crucially, we use a new pseudo-IFU cube building class in post-processing, as this observing strategy is not supported by the default STScI pipeline. The steps are described below.

##### 1. Stage 1

Stage 1 (out of 3) of the JWST Science Calibration Pipeline (the “calwebb\_detector1” module) applies detector-level corrections for all groups, transforming the data into usable slope images. To improve the identification and treatment of artifacts (e.g., snowballs and other cosmic ray traces; Green & Olszewski 2020), we modify the default values of the following parameters in the jump detection step:

```
expand_large_events=True,
sat_required_snowball = False,
min_jump_area = 10.
```

A default value for the parameter controlling the expansion of the number of pixels flagged around large cosmic ray events: snowballs, is kept ‘True’ (*expand\_large\_events*). To enhance data processing efficiency, JWST’s onboard hardware averages or drops frames to create groups. This can lead to the snowball detection algorithm missing saturated cores occurring between frames within a group, resulting in delays in accurate snowball detection (section 3.5 in JWST technical report). To address this issue, we set *sat\_required\_snowball* to ‘False’ (default = ‘True’) and increase the default minimum number of pixels (*min\_jump\_area* = 5) to 10. This bypasses the need for presence of saturated pixels within the defined jump circle and triggers the algorithm expanding the area around snowballs. The combination of these parameters leads to a successful detection and treatment of snowball events. We refer readers to this JWST technical report for a detailed discussion.

The output is a corrected 2D count rate slope image in units of counts/s. The count rate files are used as input for remaining stages of the pipeline.

##### 2. Pre-processing: $1/f$ noise correction

While the NRSIRS2 readout mode is designed to mitigate  $1/f$  read noise in the NIRSspec detectors,



some correlated noise remains in the form of vertical stripes and edge effects. We use the NSClean algorithm with its default settings (as detailed in Rauscher 2023) to remove the residual noise. In the manual mask design, Rauscher (2023) selects all spectral traces and illuminated pixels, then inverts the selection to create a background model. Background pixels are weighted to address uneven sampling, with fewer unilluminated pixels between spectral traces and greater prevalence at the top/middle/bottom of each count rate file. This produces output count rate files with uniform and nearly complete removal of correlated noise (see JWST documentation).

### 3. Stage 2

Stage 2 (“calwebb\_spec2”) of JWST’s Science Calibration Pipeline is dedicated to spectroscopic data refinement. Stage 2 applies further instrument-level corrections to slope images, generating calibrated exposures. Our customized processing includes the following steps from this stage: WCS assignment, MSA flagging, extraction of 2D arrays from spectral images, flat field and barshadow correction, flux calibration, and resampling. We do not include the standard pathloss correction step, and instead perform it in post-processing, which we explain in more details in Step 4.iii.

### 4. Stage 3 and post-processing

i. In Stage 3 (“calwebb\_spec3”) we perform only the resampling step to create final rectified and combined 2D spectra for each target from calibrated exposures. This step involves taking 2D spectra from each individual detector, resampling them using WCS and distortion information, and combining them into a single undistorted 2D spectrum for each target.

ii. A number of outliers, including cosmic rays and other artifacts (e.g., hot pixels) are apparent in the processed 2D spectra, the treatment of which remains an open issue in the standard pipeline. To remove the outliers we apply the astro-SCRAPPY<sup>2</sup> cosmic ray cleaning code, which is based on the L.A.Cosmic algorithm (van Dokkum 2001).

iii. The role of the pathloss correction function is to account for geometrical and diffraction losses of light. Pathloss correction in the standard pipeline

relies on theoretical optical models to correct for pathloss effects for non-centered point sources and those uniformly filling the slit (Ferruit et al. 2022). The current implementation of pathloss correction in the STScI reduction pipeline performs only for a standard number of slitlets (one and three). As the targets in our program are often observed with  $>3$  slitlets, we perform this correction outside of the standard pipeline. We assume a uniformly illuminated slit to correct pathloss effects for extended sources in our slit-stepping program (Nanayakkara et al. 2023). We extract a 1D pathloss function from the pipeline’s uniform pathloss reference file, and correct the 2D spectra of all exposures considering the relevant wavelength range for each target (due to the pathloss model wavelength dependence).

### 5. Cube construction

Our slit stepping pattern, as described in Section 2.2, consists of 9 dispersion “steps” ( $0''.2$  each) and 7 cross-dispersion dithers ( $0''.075$  each). Our cube building process combines the 63 individual pointings into a 3D data cube for each target. We first combine 2D spectra in the cross dispersion direction to produce a single 2D spectral slice at each step. We resample individual 2D spectra from each of the 7 dithered exposures (at each dispersion step) onto a common grid with finer spatial pixel scale, such that original pixels are Nyquist sampled. We then take the median of all exposures (with 7 exposures in the central regions, and fewer in the outer  $0''.45$ ). A median combination is used to minimize residual effects from cosmic rays, bar shadows, alternating column noise, and other artifacts. This is sufficient for the results presented herein, and this key processing step can be updated with an outlier-rejected weighted mean or other optimized algorithm following future improvements to the earlier pipeline stages. The combination of individual steps is straightforward: we append the 2D spectra at each of the 9 steps into a 3D data cube, with 9 spaxels of  $0''.2$  in the dispersion direction. The Nyquist sampled cross-dispersion spectra can be rebinned to the original pixel scale, resulting in  $0''.1 \times 0''.2$  spaxels. For analysis and display purposes in this paper, we instead interpolate the data to square spaxels of  $0''.08 \times 0''.08$ . This spaxel size corresponds to 0.7 kpc at redshifts  $z = 1-1.7$ .

<sup>2</sup> astro-SCRAPPY: <https://zenodo.org/record/1482019>

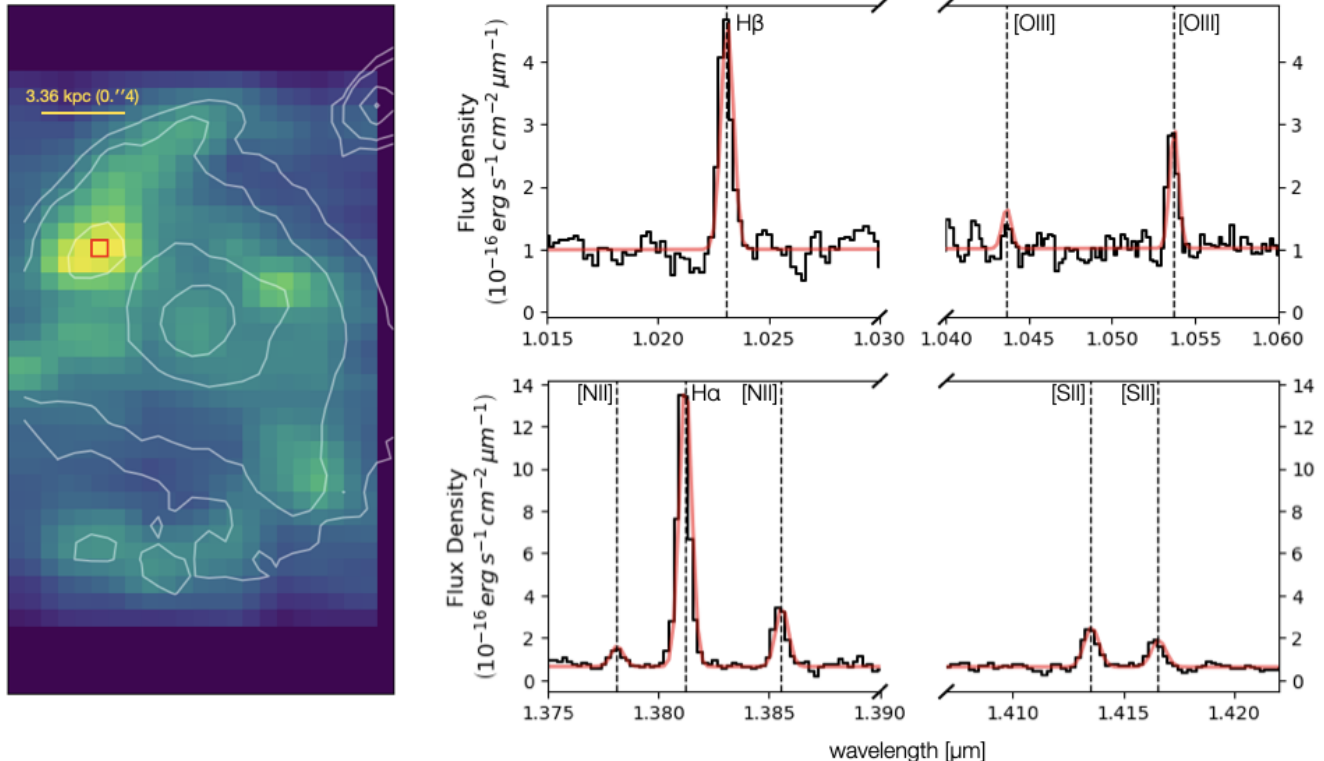


**Figure 3:** The left panel features a collapsed 2-dimensional image from the data cube centered around the  $\text{H}\alpha$  line at rest-frame  $\sim 6563 \text{ \AA}$ . Overlaid white contours indicate the galaxy continuum morphology observed in JWST/NIRCAM F444W imaging. We note that the bright continuum source in the upper-right corner is not associated with the main spiral galaxy; our slit-stepping data spectroscopically confirm it at a slightly lower redshift  $z = 1.066$ . The right panels present the 1-dimensional spectrum of a single bright spaxel (shown with the red square at left), zoomed in around the key diagnostic emission lines:  $\text{H}\beta$ ,  $[\text{O III}]$ ,  $[\text{N II}]$ ,  $\text{H}\alpha$ , and  $[\text{S II}]$ . Fits to the emission lines are shown in red and are described in the text. All key lines are well detected. Spatial mapping of these emission lines enables characterization of the kinematics, gas-phase metallicity and radial gradients, dust attenuation, star formation rate profile, and nuclear activity in this galaxy. We note that this is only one example of the 43 galaxies observed with our slit-stepping program.

The results in this paper are based on spatially resolved measurements of the strong rest-frame optical nebular emission lines. The angular resolution is limited by NIRSpec/MSA which undersamples JWST’s point spread function (PSF), especially in the dispersion direction with  $0''.2$  slitlet width. For the galaxy analyzed in this work, we achieve  $\text{S/N} > 5$  in the  $\text{H}\alpha$  emission line for individual spaxels spanning  $\sim 2''.5$ , with all additional targeted lines ( $[\text{N II}]$ ,  $[\text{S II}]$ ,  $\text{H}\beta$ ,  $[\text{O III}]$ ) well-detected in bright individual spaxels. The  $\text{H}\alpha$  narrowband flux map and example emission line detections from a single spaxel are shown in Figure 3.

We fit the emission lines within each spaxel using Gaussian profiles, which provide a good fit. The  $\text{H}\alpha$ ,  $[\text{N II}] \lambda\lambda 6548, 6585$ , and  $[\text{S II}] \lambda\lambda 6717, 6732$  lines are jointly fit with a five-component model plus a linear continuum. All lines are assumed to have the same velocity ( $V$ ) and velocity dispersion ( $\sigma$ ). The flux of each line

is a free parameter, except for the  $[\text{N II}]$  doublet whose flux ratio is fixed to the theoretical value of 2.942. The  $\text{H}\beta$  and  $[\text{O III}] \lambda\lambda 4960, 5008$  lines are similarly fit with a three-component model with the  $[\text{O III}]$  doublet flux ratio fixed to 2.984. Example maps of the  $\text{H}\alpha$  flux, velocity, and velocity dispersion are shown in Figure 4. The velocity dispersion  $\sigma_{obs}$  is corrected for NIRSpec’s spectral resolution ( $R \sim 2700$  for the G140H grating) by subtracting the line spread function FWHM in quadrature from the best-fit Gaussian FWHMs. We obtained the instrumental FWHM  $\simeq 5.2 \text{ \AA}$  by interpolating the G140H resolution curve across the wavelength range of emission lines used here. In this work we adopt a systemic redshift  $z_{sys} = 1.10417 \pm 0.00018$  corresponding to the central region of the galaxy. Velocities in Figure 4 are shown relative to this redshift.

### 3. PHYSICAL PROPERTIES

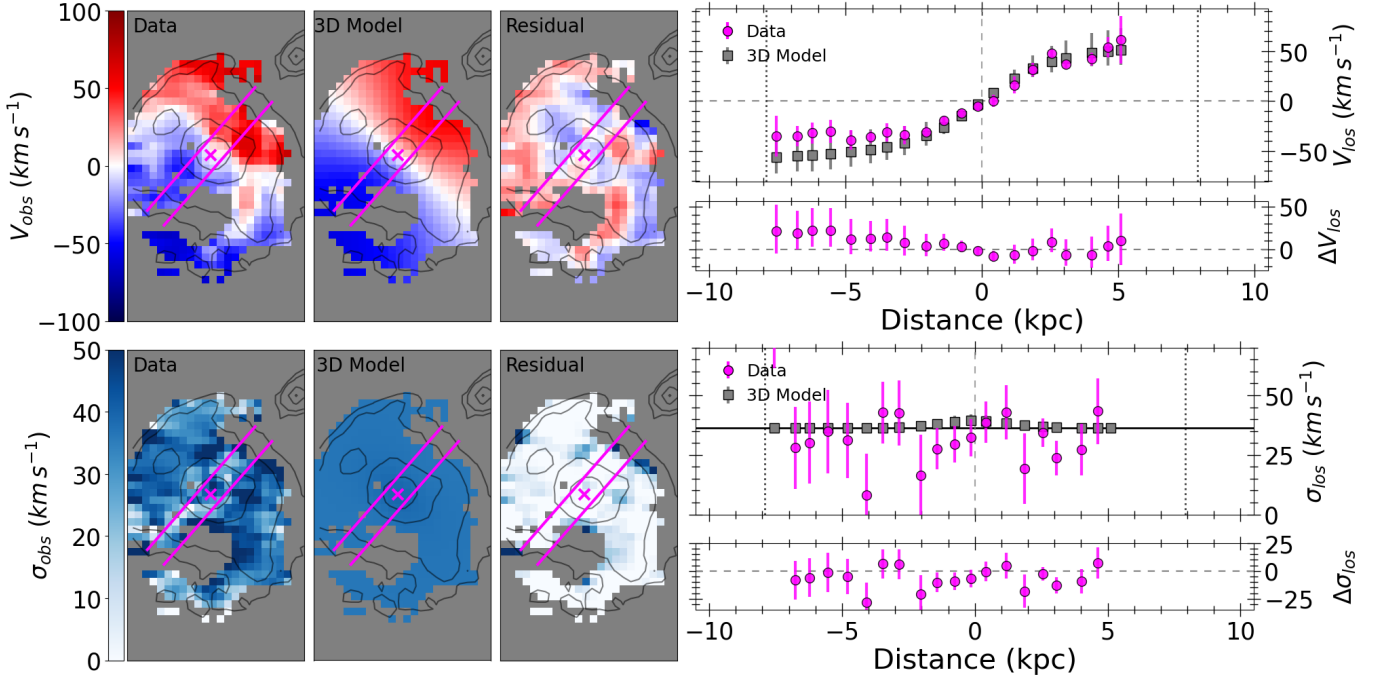


**Figure 4:** Kinematic measurements and best-fit disk model of the target galaxy. The *left panels* show: velocity  $V_{obs}$  and velocity dispersion  $\sigma_{obs}$  measured from a joint fit to H $\alpha$  and surrounding lines in each spaxel (*left*), the corresponding  $V$  and  $\sigma$  maps from our best-fit disk model (*center*) and the residuals (*right*). The kinematic center of the disk model is marked with a magenta ‘x’, and is located near the central continuum flux density peak in the F444W filter (shown with contours in each panel). Magenta lines show the location of a pseudo-slit along the kinematic major axis, from which we extract the 1-dimensional rotation curve and velocity dispersion (*right panels*). For the 1-D curves we similarly show the measured data, best-fit model, and residuals ( $\Delta V$  and  $\Delta\sigma$ ). Overall the disk model provides a good fit to the observed data, supporting that the nebular emission arises from a rotating disk viewed nearly face-on. The model residuals are  $\lesssim 20 \text{ km s}^{-1}$  and comparable to the measurement uncertainties, as can be seen in the right panels. The high angular resolution and face-on nature of this system provide an excellent measurement of the local velocity dispersion  $\sigma$ .

### 3.1. Disk Kinematics

We derive kinematic properties using GalPaK (Bouché et al. 2015), a fitting software optimized for IFU data. We fit the observed H $\alpha$  emission in the example target galaxy via forward modeling of galactic disk models, accounting for the line-spread function (LSF) and point-spread function (PSF). The LSF is assumed to be a Gaussian of FWHM  $\approx 5.2 \text{ \AA}$  based on NIRSpc documentation, and the PSF is estimated as an elliptical Gaussian with FWHM =  $0''.08 \times 0''.2$ , accounting for undersampling by the  $0''.2$  MSA slitlets. In this paper we assume a rotating disk geometry with a thickness of scale height  $h_z$ . The rotation curve is modeled as an arctangent function (Courteau 1997):

$$V(r) = \frac{2}{\pi} V_{max} \sin(i) \arctan\left(\frac{r}{r_t}\right) \quad (3)$$

where  $r$  is the distance along the major axis of the galaxy in the plane of the sky,  $V_{max}$  is the asymptotic velocity in the plane of the disk,  $i$  is the inclination of the disk, and

$r_t$  is the turnover radius. We also model the total line-of-sight velocity dispersion,  $\sigma_{tot}$ , which in general has three components added in quadrature: a local isotropic velocity dispersion  $\sigma_d$  from the self-gravity of the disk, which is given by  $\sigma_d(r) = h_z V(r)/r$  for a compact thick disk; a mixing term  $\sigma_m$  due to the mixing of velocities along the line of sight in a disk with non-zero thickness; and an intrinsic velocity dispersion  $\sigma_0$  (assumed to be isotropic and spatially constant), which represents the dynamical ‘hotness’ of the disk.

Given the rich spiral morphology of H $\alpha$  emission, which differs somewhat from the broad-band continuum (Figure 3), we do not model the full 3D flux distribution in the data cube. Instead we fit the velocity and dispersion maps measured from H $\alpha$  and the surrounding metal lines as discussed in Section 2.5. We use GalPaK to construct model 2D maps of the velocity and dispersion, and perform a Markov chain Monte Carlo (MCMC) parameter space exploration with the Python software emcee (Foreman-Mackey et al. 2013). A Gaus-

sian prior is adopted for the center of the galaxy, using the position of peak stellar continuum flux in the NIR-Cam F444W image. The F444W filter corresponds to rest-frame K band ( $\sim 2.1 \mu\text{m}$ ) which is expected to be a good tracer of the stellar mass distribution (e.g., Bell & de Jong 2001). For all other parameters we adopt a flat prior (including, e.g.,  $V_{max}$  and  $\sigma_0$ ). The likelihood function for our model is defined by agreement with the measured velocity  $V$  and dispersion  $\sigma$  maps:

$$\log \mathcal{L} \sim -0.5 \times \sum_{X \in \{V, \sigma\}} \sum_j \left( \frac{X_{obs,j} - X_{model,j}}{Err_{X,j}} \right)^2 \quad (4)$$

which sums over all spaxels ( $i$ ) in both  $V$  and  $\sigma$ . Here  $X_{obs}$ ,  $X_{model}$ , and  $Err_X$  are the 2D maps of the data, extracted model, and standard deviation measurement uncertainty, respectively. The best-fit  $V_{model}$  and  $\sigma_{model}$  maps along with the residuals ( $X_{obs} - X_{model}$ ) are shown in Figure 4. We also show 1D rotation and velocity dispersion curves extracted along the best-fit major axis.

Overall the disk model provides a good fit to the kinematic measurements. The residuals are  $\lesssim 20 \text{ km s}^{-1}$  for both  $V$  and  $\sigma$ . The best-fit inclination  $i = 12.9^{+2.7}_{-1.1}$  degrees is nearly face on, which is also clear from the imaging data. We note that the source morphology was not used to constrain the fit, such that the model provides an independent confirmation of the face-on disk geometry. While the line-of-sight rotational velocity  $V_{max} \sin(i)$  is tightly constrained by the data, the large inclination correction factor (i.e.,  $\frac{1}{\sin(i)} \simeq 4.5$ ) makes  $V_{max} = 290 \pm 40 \text{ km s}^{-1}$  and  $V/\sigma = 8.1 \pm 1.5$  relatively uncertain. As such we refrain from detailed analysis of the rotation curve and dynamical mass profile in this galaxy. We note that the  $V/\sigma$  value is characteristic of well-settled disks, and agrees well with predictions from the TNG50 simulation at this redshift and stellar mass (Pillepich et al. 2019). Such high values of  $V/\sigma$  are also found in the FIRE zoom-in simulations after disk settling (Stern et al. 2021; Gurvich et al. 2023). The majority of our targets have a higher (more edge-on) inclination which allows better constraints on the circular rotation velocity. On the other hand, the velocity dispersion  $\sigma_0 = 36^{+5}_{-4} \text{ km s}^{-1}$  is determined with good precision, and this is the key quantity which describes the dynamical state of the disk (e.g., cold thin disk vs. turbulent thick disk). The  $H\beta$  and  $[\text{O III}]$  emission lines give consistent results. In this case the  $\sigma$  value observed from a nearly face-on inclination corresponds closely with the vertical component of velocity dispersion, which sets the disk scale height.

In Figure 5 we compare  $\sigma_0$  for the galaxy studied here with average values compiled from various surveys as a

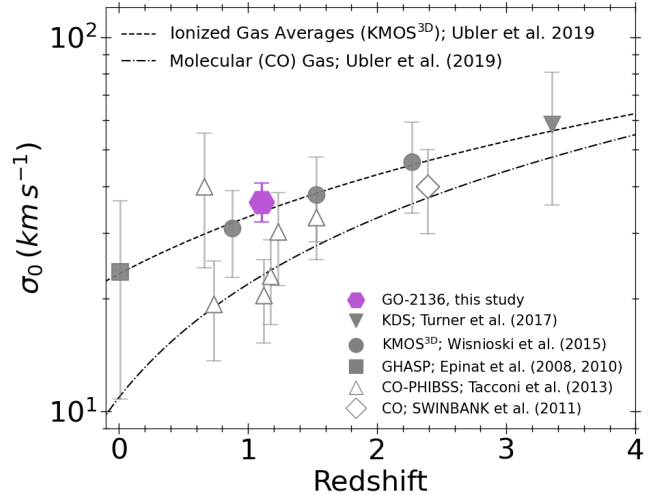


**Figure 5:** Velocity dispersion measured for our galaxy (violet hexagon) compared to previous observational results spanning redshifts up to  $z \lesssim 4$  (KDS: Turner et al. 2017; KMOS-3D: Wisnioski et al. 2015; GHASP: Epinat et al. 2008, 2009; PHIBBS: Tacconi et al. 2013; Swinbank et al. 2011). We show the approximate redshift evolution separately for ionized gas such as  $H\alpha$  (filled symbols) and molecular gas traced by CO (open symbols). We show the average redshift evolution curves for ionized (dashed) and molecular gas (dash-dotted) from Übler et al. (2019). Our measurement from JWST slit-stepping data aligns well with the average ionized gas measurements at  $z \sim 1$ .

function of redshift. Despite the clear spiral disk morphology, the measured  $\sigma_0$  is higher than for typical spiral galaxies at  $z \simeq 0$ , and comparable to the largest values found in the GHASP sample (Epinat et al. 2008). However we find excellent agreement with the average trend seen in KMOS<sup>3D</sup> (Wisnioski et al. 2015) and other kinematic surveys of ionized gas (e.g., Simons et al. 2017). While this is only a single object whose properties may not be representative, it appears to support the picture of velocity dispersion increasing with redshift. Our best-fit  $\sigma_0$  may slightly underestimate the true value due to possible slit illumination effects. Our analysis assumes uniform slit illumination, whereas a partial illumination (e.g., with bright nebular emission concentrated on one side of the  $0.2$  slit) would cause the line widths (e.g.,  $\sigma$ ) to appear smaller. Such an effect could cause variation in both the measured  $\sigma$  and  $V$ , along with larger scatter in line widths potentially reaching values smaller than the assumed instrument resolution. We would also expect the velocity dispersion measured from  $H\beta$  to be systematically smaller than  $H\alpha$  in the presence of non-uniform slit illumination (due to the smaller PSF at

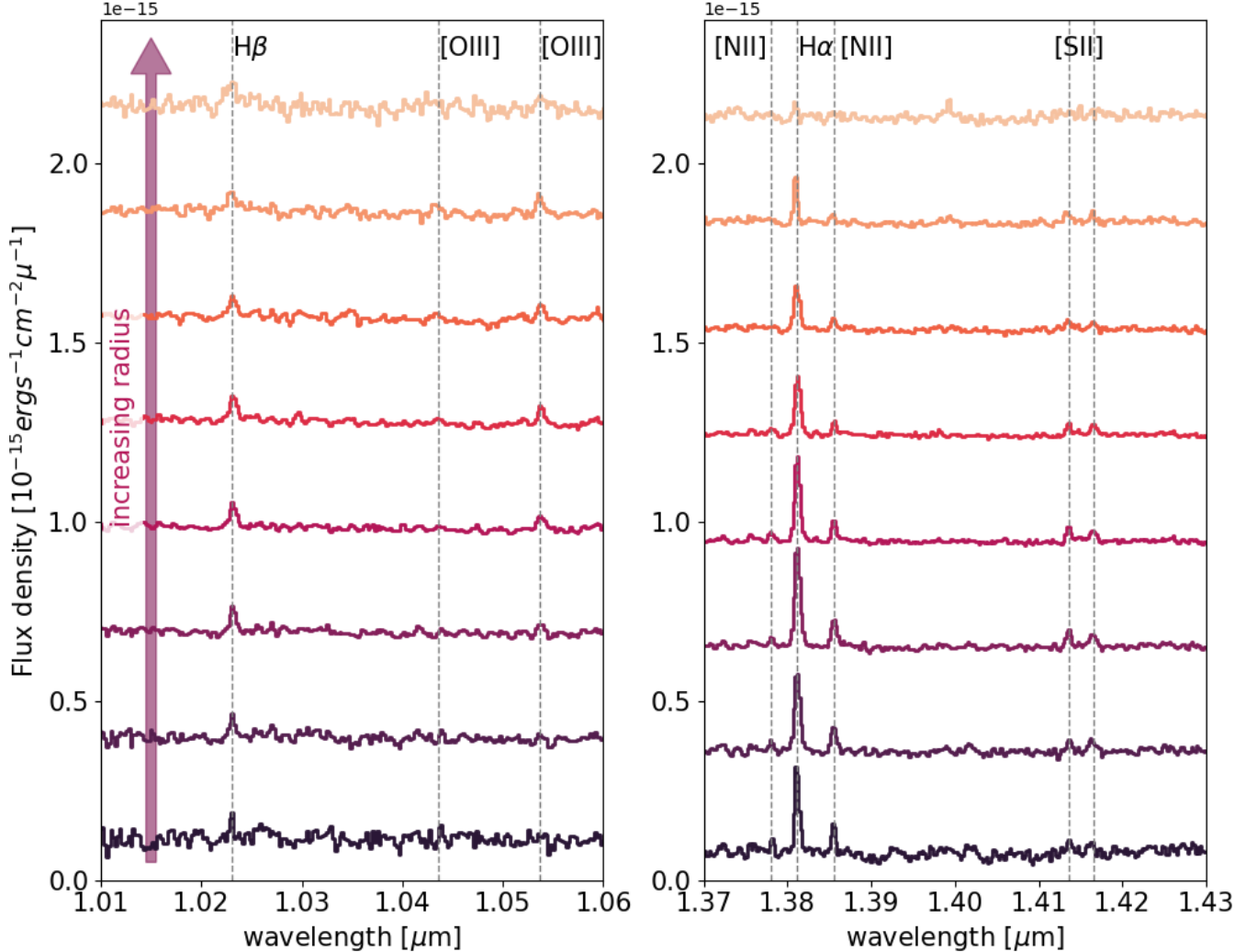


**Figure 6:** Average flux density per spaxel in each radial bin. Successive bins are offset vertically for display purposes, extending from the galaxy’s center (bottom spectra) to the outermost bin at  $\sim 13$  kpc (top-most spectra), as indicated by the arrow at left. The bins are constructed from deprojected galactocentric radius as described in the text, with a bin width of 1.7 kpc ( $0''.2$ ). The outermost bin is not used in our analysis due to low S/N of the emission lines. Vertical gray dashed lines highlight the main diagnostic emission lines of  $H\beta$ , [O III], [N II],  $H\alpha$ , and [S II]. We observe a clear radial trend in emission line ratios, with [N II]/ $H\alpha$  decreasing and [O III]/ $H\beta$  increasing at larger radii. This is explained by a smooth gas-phase metallicity gradient as described in Section 3.3.

shorter wavelengths). Instead we find relatively small scatter in velocity dispersion, with values from  $H\beta$  and [O III] being slightly larger on average (by  $13 \pm 11\%$ ) than those measured from  $H\alpha$  in radial bins. We thus conclude that the bias from non-uniform slit illumination is comparable or smaller than the measurement uncertainty. Future efforts may be able to better quantify the effects of non-uniform slit illumination by forward-modeling the light distribution (e.g., based on imaging or grism spectroscopy).

In summary we find that the dynamical state of the disk, as indicated by local velocity dispersion, is more

turbulent than in  $z \sim 0$  spirals and comparable to that inferred from large ground-based samples at  $z \sim 1$  (e.g., Wisnioski et al. 2015; Stott et al. 2016). In contrast to typical ground-based data, our measurement of  $\sigma_0$  is especially robust to beam smearing effects, thanks to the nearly face-on inclination and the exquisite space-based point-spread function of the data. The best-fit kinematic major axis (PA = 139 degrees) and disk inclination ( $i = 12.9$  degrees) are used to construct deprojected radial bins in the following sections.

### 3.2. Flux Ratios and BPT Diagram

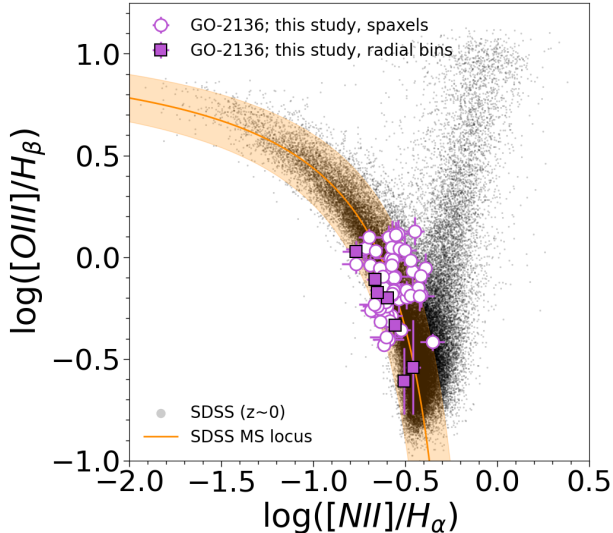


**Figure 7:** BPT diagram of the  $[\text{O III}]/\text{H}\beta$  versus  $[\text{N II}]/\text{H}\alpha$  flux ratios, with measurements for both individual spaxels (open circles) and radial bins (filled squares). These are overlaid on a large sample of  $z \sim 0$  galaxies from the Sloan Digital Sky Survey (SDSS; Abazajian et al. 2009). The star-forming locus described by Kewley et al. (2013) is shown with the orange line and shading, while the AGN sequence extends to the upper right. Both the individual spaxels and radial bins for our target galaxy consistently lie along the locus of star-forming galaxies, with radial trends indicative of metallicity gradients (see Section 3.3). Based on this BPT diagnostic, we do not detect any signature of an AGN in this target; nebular emission is dominated by star forming regions even within the central resolution element.

To classify the dominant energy source of line emission within this galaxy and to establish the degree of nuclear supermassive black hole activity, we examined the Baldwin–Phillips–Terlevich (BPT) diagram (Baldwin et al. 1981) of  $[\text{O III}]/\text{H}\beta$  versus  $[\text{N II}]/\text{H}\alpha$  flux ratios. Given the moderate S/N of  $[\text{O III}]$  and  $\text{H}\beta$  emission within typical individual spaxels, we use radial annular bins. The bins are constructed using the deprojected radius based on the best-fit inclination and position angle derived from our kinematic disk model (Section 3.1). We adopt bins of 1.7 kpc ( $0''.2$  arcseconds) in deprojected radius, corresponding to the MSA slit width. We stack the spectra in each bin and fit the emission profiles to calculate the radially averaged flux ratios across the galaxy. We verified that the fit residuals are in good agreement with the estimated error spectra. Figure 7 shows the resulting BPT diagram measured for both radial bins and individual bright spaxels throughout the galaxy. For

individual spaxels shown in the BPT diagram in Figure 7 we adopt a threshold of  $\text{S/N} \geq 5$  in all requisite lines, exclude spaxels near the edges and those far outside the boundary of the galaxy as indicated by F444W photometric contours, and exclude spaxels with velocity or dispersion measurements near the fitting boundaries (indicating spurious fits).

Our data show that nebular emission within this galaxy is dominated by star formation, as all spatially-resolved regions lie well within the star-forming locus of the BPT diagram. The galaxy follows the star-forming locus within radial bins, and we can also clearly verify that prominent “clumps” of  $\text{H}\alpha$  emission seen in Figure 3 are indeed driven by active star formation. Notably the PSF of JWST allows us to resolve the central  $R \lesssim 0.8$  kpc with minimal beam smearing from emission at larger radii. We see no evidence of AGN contribution even within this central resolution element. We can place a rough limit on the contribution of nuclear emission driven by supermassive black hole accretion: assuming a central AGN with a flux ratio  $\log([\text{O III}]/\text{H}\beta) = 0.5$ , a contribution of 20% of the Balmer line fluxes from such an AGN in the central resolution element would be readily detected (approximately tripling the  $[\text{O III}]$  flux relative to the star-forming locus in the central resolution element). The central bin contains only  $\simeq 3.8\%$  of the total observed  $\text{H}\alpha$  flux (although a larger fraction of total intrinsic flux accounting for attenuation; see Section 3.4). Taking 20% of this, we arrive at a conservative estimate that  $\lesssim 0.8\%$  of the total observed  $\text{H}\alpha$  flux could be associated with an AGN. The corresponding limit on the central spatial resolution element is approximately half of this ( $\lesssim 0.4\%$ ). We conclude that either there is very little supermassive black hole accretion in this galaxy, or that any accretion-driven luminosity must be heavily dust-obscured. This sensitive limit highlights the power of high angular resolution observations to detect low-luminosity AGN (e.g., Wright et al. 2010) even in galaxies dominated by star formation.

### 3.3. Gas-Phase Metallicity Gradient

We now turn to the gas-phase metallicity as a function of radius using the same bins described in Section 3.2. We estimate metallicity using the locally calibrated strong-line relations of Pettini & Pagel (2004, PP04) and Curti et al. (2017, C17) using the available  $[\text{N II}]/\text{H}\alpha$  and  $[\text{O III}]/\text{H}\beta$  line ratios. Specifically we consider the

$$\text{N2} = \log([\text{N II}] \lambda 6584/\text{H}\alpha),$$

$$\text{R3} = \log([\text{O III}] \lambda 5007/\text{H}\beta), \text{ and}$$

$$\text{O3N2} = \log \left( \frac{[\text{O III}] \lambda 5007 / \text{H}\beta}{[\text{N II}] \lambda 6584 / \text{H}\alpha} \right) = \text{R3} - \text{N2}$$

diagnostics. While numerous other calibrations are available in the literature, including some based directly on galaxies at similar  $z \sim 1$  (Jones et al. 2015a; Sanders et al. 2020), the adopted calibration has little effect on the conclusions of this section. We use PP04 and C17 in order to illustrate both the numerical differences and qualitatively similar conclusions.

In Figure 8 we show the gas-phase metallicity  $12 + \log(\text{O}/\text{H})$  as a function of deprojected radius (using the mean radius of spaxels within each bin). The top panel plots results from all three diagnostics (O3N2, N2, and R3) using the C17 calibrations. All show similar negative gradients, reflecting the radial trends in emission line flux ratios apparent in Figures 6 and 7. We additionally show a linear fit for the O3N2 index, which gives a best-fit gradient slope  $\Delta \log(\text{O}/\text{H}) / \Delta R_d = -0.020 \pm 0.002 \text{ dex kpc}^{-1}$ . The independent N2-based measurement differs systematically in normalization by  $\sim 0.05$  dex, while R3-based measurement is consistent with the O3N2-based measurement. Both are within the known scatter in these relations (e.g., Kewley et al. 2019), and display a consistent gradient slope. Independent line ratios thus give a consistent overall metallicity and radial gradient.

In the lower panel of Figure 8 we make a direct comparison with typical metallicity gradients measured for  $z \sim 0$  spiral galaxies by Belfiore et al. (2017), at the *same stellar mass range* ( $\log M_*/M_\odot = 10\text{--}10.5$ ) as our target galaxy ( $\log M_*/M_\odot = 10.3$ ). For consistency we compare results from the same metallicity calibration (i.e., O3N2 from PP04), normalized to the effective radius  $R_d/R_{\text{eff}}$  (with  $R_{\text{eff}} = 4.82 \text{ kpc}$  for our target; Section 3.5). The PP04 calibration gives a larger total O/H range and steeper metallicity gradient compared to C17, while we emphasize the conclusion of a negative radial gradient remains robust.

The observed metallicity gradient is in accordance with the kinematic results which indicate a well-ordered rotating disk. Gas mixing due to turbulence, mergers, feedback-driven galactic fountains, or other factors is expected to reduce or eliminate any radial gradient (e.g., Ma et al. 2017; Rich et al. 2012; Kewley et al. 2010). The strong gradient in this galaxy implies little influence from such effects. At fixed stellar mass  $\log M_*/M_\odot = 10.3$ , the metallicity gradient of our example galaxy at  $z = 1.1$  is steeper (more negative slope) than the average at  $z \sim 0$  from Belfiore et al. (2017) while both have similar central metallicities. However we caution that the  $z = 1.1$  galaxy is a case study and is not necessarily representative of the general population.

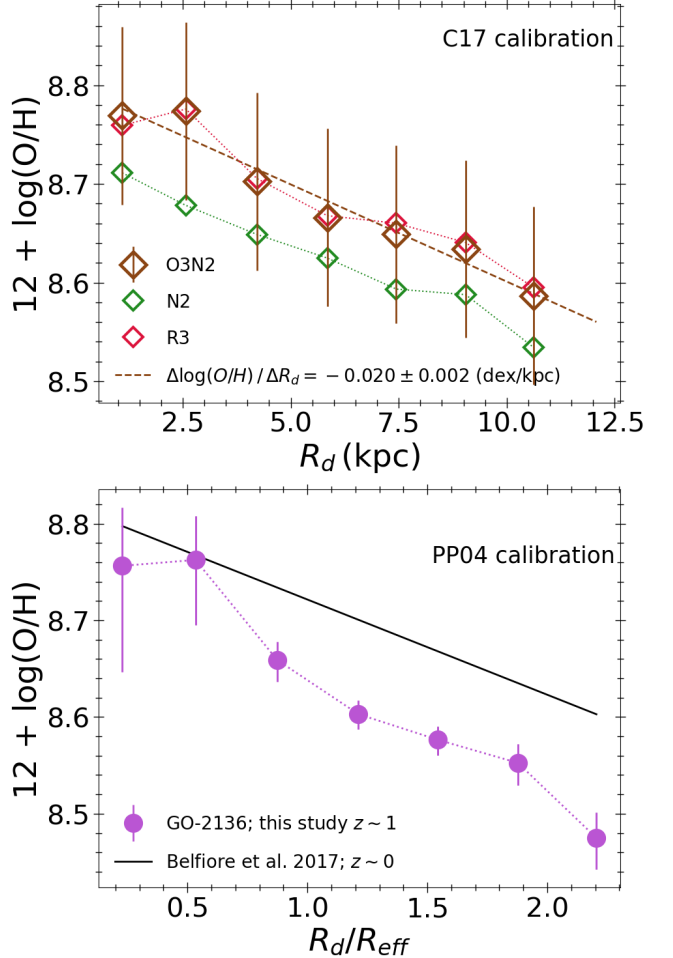


**Figure 8:** Gas-phase metallicity as a function of radius, showing a clear radial metallicity gradient in the target galaxy. The *upper panel* presents the metallicity gradient based on three different strong-line diagnostics from Curti et al. (2017, C17) along with the best-fit gradient for O3N2 as described in the text. We observe similar gradients in each diagnostic, including the independent N2 and R3, with differences smaller than the scatter in the calibrations. As an example, error bars show the 0.09 dex scatter in the O3N2 calibration. The *lower panel* shows the metallicity gradient using the O3N2 calibration from Pettini & Pagel (2004, PP04), with radius normalized to  $R_{\text{eff}}$  as opposed to physical radius in the upper panel. Error bars show the  $1\sigma$  statistical uncertainty (neglecting scatter in the calibration), and we note that relative uncertainty in the other diagnostics is smaller than for O3N2. We compare this result directly to the average gradients of  $z \sim 0$  disk galaxies of similar stellar mass measured by Belfiore et al. (2017). Relative to nearby galaxies at fixed mass, the  $z \sim 1$  target galaxy has a steeper gradient (in units of  $\text{dex } R_{\text{eff}}^{-1}$ ) and similar central metallicity.

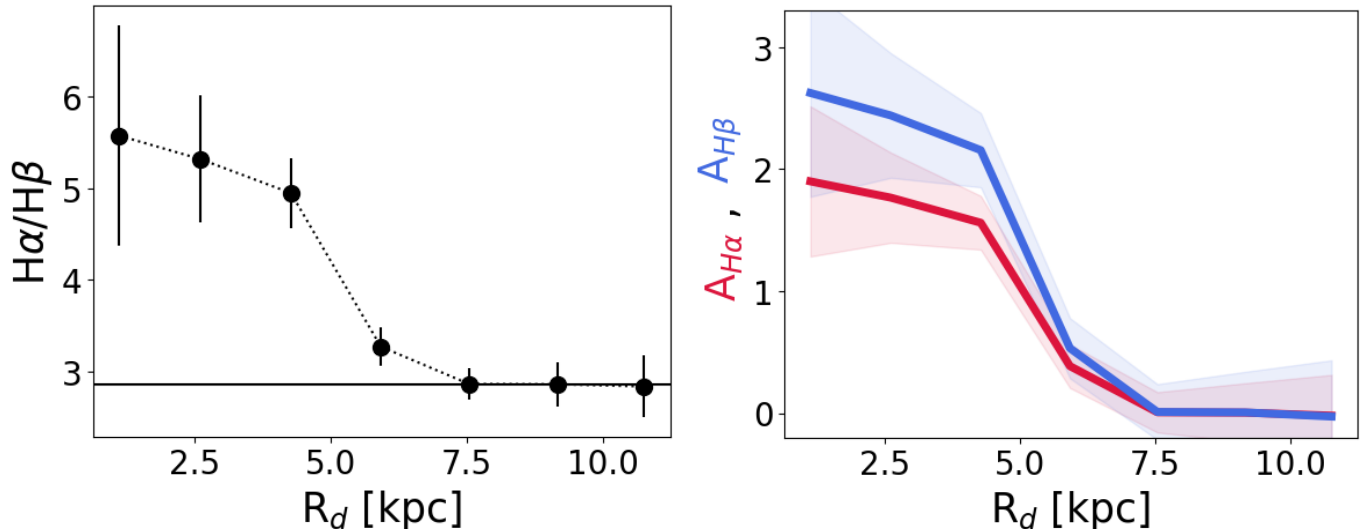


**Figure 9:** The left panel shows the measured radial Balmer decrement profile (defined as the ratio of  $H\alpha$  and  $H\beta$  emission line fluxes), which is used to derive dust attenuation profiles for  $H\alpha$  and  $H\beta$  (red and blue curves, respectively, in the right panel). A negative radial trend in the Balmer decrement is evident, with high values in the inner  $\lesssim 4$  kpc indicating a significant level of optical obscuration in these regions. In contrast the outer disk at radii  $\sim 10$  kpc is consistent with no attenuation.

Its SFR places it below the main sequence at  $z \sim 1$  (Figure 1), such that stellar feedback and other gas-mixing process may be relatively modest. Preliminary analysis indicates that it is in the steepest quartile of dex  $R_{eff}^{-1}$  gradient slopes within the sample observed by this program (Ju et al., *in prep*). We also note that this is not an evolutionary comparison, as our target galaxy is expected to grow more massive by  $z \sim 0$ . We leave a detailed analysis of our full sample and its chemical evolution for future work; here we have demonstrated the ability to measure metallicity gradients at a precision suitable for comparison with  $z \sim 0$  galaxies.

### 3.4. Dust Attenuation Gradient

Optical H I emission lines are a valuable diagnostic for characterizing dust attenuation in galaxies. The Balmer decrement, defined as the ratio of  $H\alpha/H\beta$ , is a commonly used metric to determine the degree of attenuation and reddening (e.g., Charlot & Fall 2000). The attenuation is determined by quantifying its deviation from the theoretical value (Baker & Menzel 1938; Osterbrock & Ferland 2006). Assuming Case B recombination with electron temperature  $10^4$  K and electron density of  $10^2 \text{ cm}^{-3}$ , the expected Balmer decrement value is 2.86 (Osterbrock & Ferland 2006; Storey & Hummer 1995). In each radial bin, we measure the integrated  $H\alpha/H\beta$  flux ratios from the best-fit line profiles. Figure 9 shows the resulting Balmer decrement profile of the galaxy. It

displays a clear negative radial trend, indicating larger attenuation in the central regions.

We infer attenuation  $A_{H\alpha}$  and  $A_{H\beta}$  from the measured Balmer decrement following standard methods. The attenuation is related to the color excess  $E(B-V)$  as  $A_\lambda = k_\lambda \times E(B-V)$ , where  $k_\lambda$  corresponds to the reddening curve. The color excess  $E(B-V)$  can be measured from:

$$\begin{aligned} E(B-V) &= \frac{E(H\beta - H\alpha)}{(k_{H\beta} - k_{H\alpha})} \\ &= \frac{2.5}{(k_{H\beta} - k_{H\alpha})} \log_{10} \frac{(H\alpha/H\beta)_{obs}}{2.86} \end{aligned} \quad (5)$$

where 2.86 is the assumed intrinsic  $H\alpha/H\beta$  flux ratio. It is necessary to assume a reddening law for  $k_\lambda$ . For consistency with previous studies (e.g., Nelson et al. 2016b), we adopt the Calzetti et al. (2000) reddening law (with  $k_{H\alpha} = 3.33$  and  $k_{H\beta} = 4.60$ ). The resulting attenuation versus radius for both  $H\alpha$  and  $H\beta$  are shown in the right panel of Figure 9. We note that the choice of reddening law can affect the derived attenuation (e.g.,  $A_{H\alpha}$ ) – although this effect is minor in the optical wavelength range, whereas the color excess and radial profile shape are relatively robust. We find a strong radial trend with higher attenuation in the central  $\lesssim 4$  kpc. This is similar to the results for massive  $z \sim 2$  disk galaxies found by Tacchella et al. (2018) using other methods to determine attenuation.



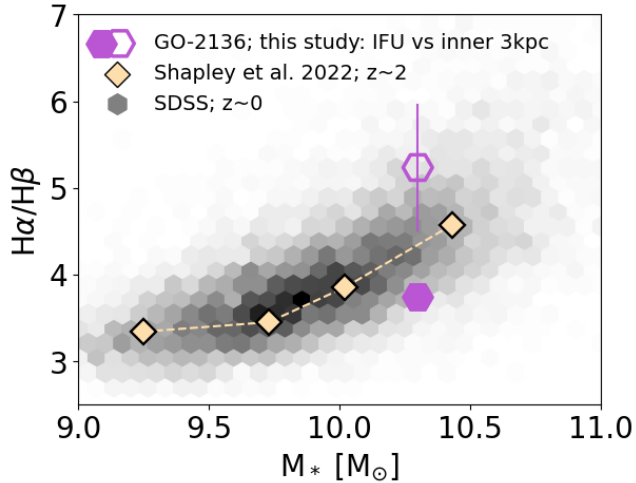


**Figure 10:** The Balmer decrement as a function of stellar mass at different redshifts. We measure the Balmer decrement from the integrated spectrum of our target  $z = 1.1$  galaxy (filled violet hexagon) and from the inner 3 kpc (open hexagon). We emphasize the significance of using data from the entire galaxy to determine the Balmer decrement, as relying solely on the central region tends to yield higher attenuation estimates due to radial gradients (Figure 9). Our overall attenuation measurements are similar to previous findings up to  $z \sim 2.5$ .

Previous studies of the Balmer decrement in galaxies have noted a positive correlation with stellar mass, suggesting that more massive galaxies typically have larger attenuation from dust in their interstellar medium (e.g. van Dokkum et al. 2005; Ly et al. 2012; Kashino et al. 2013; Domínguez et al. 2013; Price et al. 2014; McLure et al. 2018; Shapley et al. 2022). These studies also indicate no significant evolution in dust attenuation at fixed mass up to  $z \lesssim 2$ . Moreover, alternative assessments of dust attenuation through indicators such as infrared excess IRX, optical attenuation  $A_V$ , and/or ultraviolet attenuation  $A_{1600}$  and spectral slope  $\beta$  have reported consistent findings (e.g., Wuyts et al. 2013; Heinis et al. 2014; Bouwens et al. 2016; Bourne et al. 2017; Whitaker et al. 2017; McLure et al. 2018). In Figure 10 we compare the Balmer decrement of our target from both the integrated spectrum and from the central  $R_d < 3$  kpc (to mimic single-slit or fiber observations), with the results from galaxies at lower and higher redshifts ( $z \simeq 0$ : SDSS;  $z \simeq 2.3$ : MOSDEF, Shapley et al. 2022). There is a striking difference between the integrated spectrum and the central  $R_d < 3$  kpc, with the central Balmer decrement being nearly  $1.5\times$  the integrated value. This central region is representative of the area covered by a single NIRSpc slitlet (Figure 1). This comparison

shows that single-slit or otherwise centrally concentrated observations can lead to an inaccurate assessment of the overall dust attenuation in the galaxy. The integrated measurement of our galaxy exhibits a smaller Balmer decrement compared to the average observed at a fixed stellar mass in both the SDSS sample and the  $z \simeq 2.3$  MOSDEF sample, although it is within the scatter seen in SDSS. Lorenz et al. (2023) found no significant correlation between the Balmer decrement and galaxy viewing angle, suggesting that the face-on inclination of our target is not responsible for the moderately low attenuation. However they also noted a trend of attenuation increasing with star formation rate. Our target galaxy has a SFR of  $3 M_\odot \text{ yr}^{-1}$  which places it below the typical sSFR at its redshift (e.g., Whitaker et al. 2012; Figure 1), which may partly explain the lower attenuation.

### 3.5. Surface Brightness Profile

We now examine the surface density profile of star formation, as traced by attenuation-corrected  $H\alpha$  emission, and compare it with the stellar continuum. This provides insight into the structural evolution and radial size growth of this galaxy. From the measurements described in Section 3.4, we obtain intrinsic  $H\alpha$  and  $H\beta$  fluxes as a function of radius via

$$F_{intr,\lambda} = F_{obs,\lambda} \times 10^{(0.4A_\lambda)}.$$

Figure 11 shows the observed and intrinsic (i.e., attenuation corrected) radial surface brightness profiles for both  $H\alpha$  and  $H\beta$ . The observed profiles are relatively flat in the inner 5 kpc, with larger Balmer decrements indicating more attenuation in the central regions (demonstrated in Figure 9). The average spatial profiles found at  $z \sim 1.4$  by Nelson et al. (2016b) similarly show a flattening of the inner  $H\beta$  profile at high masses, with larger Balmer decrements in the central regions. However the stacked profiles in Nelson et al. (2016b) exhibit centrally peaked  $H\alpha$  profiles across all mass bins, in contrast to the flatter inner profile seen in Figure 11. The attenuation-corrected profiles of our target galaxy do show a clear central peak, with an approximately exponential surface brightness profile. This is indicative of star formation continuing to build an exponential disk. We find no indication of significant in situ bulge formation (in which case we would expect an elevated central surface brightness relative to the overall exponential profile), nor of inside-out quenching (in which case we would expect a lower corrected central surface brightness; e.g., Tacchella et al. 2018; Lin et al. 2019).

Our target is covered by JWST/NIRCam imaging from the CEERS survey (Finkelstein et al. 2023), which we use to trace the stellar surface brightness profile. Of

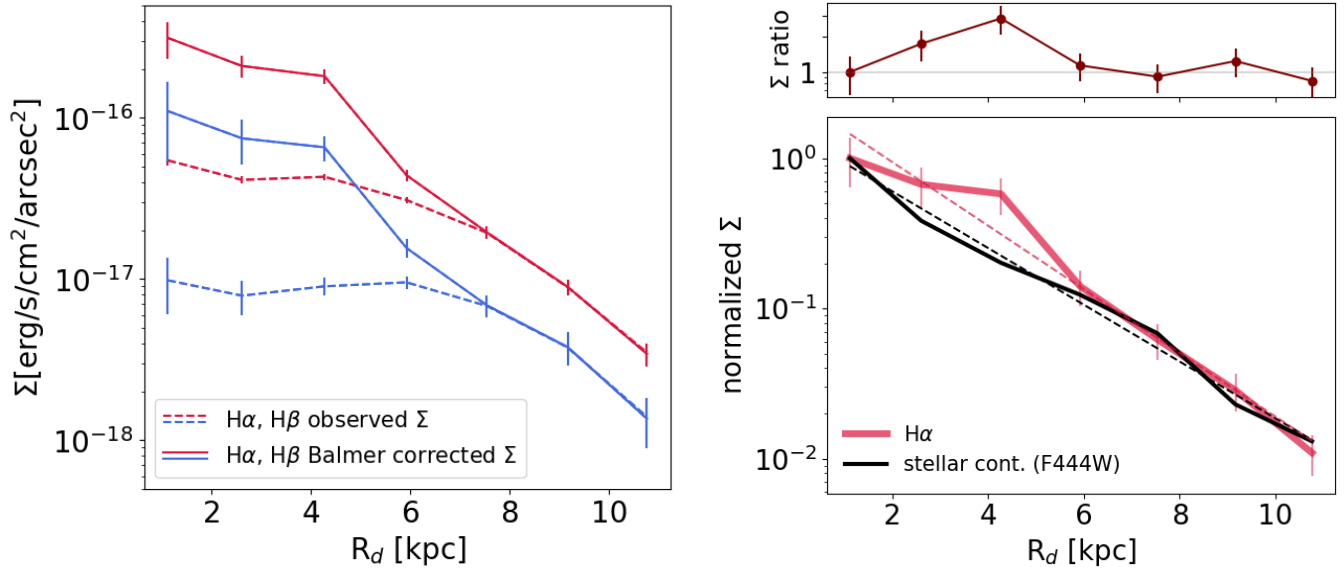


**Figure 11:** Radial surface brightness profiles  $\Sigma$  of H $\alpha$  and H $\beta$  (red and blue curves respectively) are shown in the left panel for both observed (dashed) and dust-corrected emission (solid). These profiles exhibit an approximately exponential decreasing trend with radius, with an apparent excess around 4 kpc. In the right panel, we compare the H $\alpha$  (red solid line) and infrared stellar continuum (black solid line: NIRCcam F444W filter) surface brightness profiles, normalized at their respective central bins. Exponential fits for both profiles are overlaid (dashed lines). The upper right panel presents their ratio, which corresponds approximately to the specific star formation rate. We see a clear H $\alpha$  excess at  $R_d \simeq 4$  kpc with nearly constant values elsewhere out to  $\gtrsim 10$  kpc. The similar scale lengths indicate that the star formation (traced by H $\alpha$ ) is not driving a rapid size growth of this galaxy. Instead it is adding mass to the disk approximately in proportion to the local stellar mass (traced by stellar continuum).

particular interest is the F444W band, which measures stellar continuum at a rest-frame of  $2.1 \mu\text{m}$  (i.e., rest-frame K band). We use this as a proxy for the stellar mass surface density, as the mass-to-light ratio varies by only a factor  $\lesssim 2$  at K band (e.g., Bell & de Jong 2001; McGaugh & Schombert 2014), which is minimal given the factor  $100\times$  in surface brightness probed here. The Balmer decrement profile (Figure 9) additionally suggests relatively little dust attenuation  $A_K$  at these wavelengths. The F444W image is first rescaled to the same pixel size as the NIRSpc data cube, after which we extract the radial surface brightness profile. In Figure 11 we compare the dust corrected H $\alpha$  surface brightness profile (which traces the SFR) to that of rest-frame K band stellar continuum (which traces stellar mass). Both are normalized at the central bin for ease of comparison. The H $\alpha$  and stellar continuum both follow an approximately exponential profile with similar scale length, decreasing by a factor of  $\sim 100\times$  over  $\sim 10$  kpc in radius. An exponential profile fit gives scale length  $R_s = 2.9 \pm 0.3$  kpc for the continuum, corresponding to a half-light or effective radius of  $R_{eff} = 4.8 \pm 0.5$  kpc. This is consistent with the size-mass relationship for late type galaxies at  $z \sim 1$ , which indicate typical  $R_{eff} \simeq 4$ –

5 kpc at the mass of our target (van der Wel et al. 2014). Additionally we note the half-light radius of our target galaxy is similar to that of the Milky Way ( $\sim 4$ –6 kpc; Bland-Hawthorn & Gerhard 2016; Lian et al. 2024).

The H $\alpha$  (= SFR) and continuum (= stellar mass) scale lengths are close and mutually consistent within  $1.2\sigma$ , with H $\alpha$  being  $11 \pm 9\%$  smaller than the continuum. At face value this is in contrast to the picture of “inside-out” disk growth whereby the H $\alpha$  scale length is larger than that of the stars. For example, Nelson et al. (2016a) report that H $\alpha$  scale lengths of their sample of  $z \sim 1$  galaxies are on average  $14\%$  larger than the observed  $1.4 \mu\text{m}$  continuum for similar redshift and stellar mass ( $\log M_*/M_\odot = 10$ – $10.5$ ), although  $R_{eff}$  is only  $4\%$  larger and consistent within uncertainties. While our measurements are compatible with this level inside-out growth at the  $\sim 2\sigma$  level, overall it appears that the ongoing star formation is not significantly altering the galaxy’s scale length. We conclude that this galaxy stellar component is growing proportionally more massive on average at all radii.

Figure 11 also shows the ratio of H $\alpha$  and stellar continuum radial surface brightness profiles, normalized at the central bin. This ratio is proportional to the spe-

cific SFR (sSFR). The most notable deviation from a constant sSFR profile is a clear excess of H $\alpha$  emission around 4 kpc, while elsewhere the profiles align closely. The excess reaches up to three times higher H $\alpha$  surface brightness relative to the continuum.

One possible explanation for this H $\alpha$  excess emission may be prominent clumps within the spiral arms, including a bright clump in the upper left and a fainter clump in the upper right quadrant in Figure 3. However, the Balmer decrement indicates significant dust obscuration in the inner 4 kpc, such that the morphology seen in Figure 3 differs from the more centrally-concentrated profile we obtain after attenuation correction. To further explore the nature of the excess emission at 4 kpc, we split the cube into “upper” and “lower” halves. After correcting for dust, the H $\alpha$  surface brightness density in the lower half is higher than that of the upper half (which contains the brightest observed regions). We find excess in attenuation-corrected H $\alpha$  surface brightness profiles in both halves, indicating that it is not caused solely by the discrete bright regions. Instead it may suggest the presence of a Lindblad resonance driving a ring of star formation at this radius (e.g., Buta & Combes 1996).

#### 4. DISCUSSION AND CONCLUSIONS

We have presented the design and initial results of the MSA-3D program which obtained spatially resolved spectroscopy for 43 star-forming galaxies at  $z \sim 1$ , using a slit-stepping observing strategy with JWST/NIRSpec’s MSA. We illustrate the data quality with a case study of a spiral disk galaxy at  $z = 1.104$ . This galaxy exhibits features typical of late-type spirals in the nearby universe: prominent spiral arm morphology (Figures 1, 3), rotation-dominated kinematics (Section 3.1; Figure 4), a negative gas-phase metallicity gradient (Section 3.3; Figure 8), and exponential surface brightness profiles in both stellar continuum and star formation (Section 3.5; Figure 6). These results collectively demonstrate the ability of our slit-stepping methodology to characterize  $z \gtrsim 1$  galaxies via emission line mapping with  $\sim 1$  kpc resolution. We emphasize that the galaxy analyzed in detail in this paper is typical of the data quality within the larger sample. We refer readers to Ju et al. (*in prep*) for analysis of the metallicity gradients measured for 26 of our 43 targets, as well as maps of the H $\alpha$  flux and kinematics.

The quality of emission line measurements we achieve with MSA-3D at  $z \sim 1$  is comparable to that of MaNGA (Bundy et al. 2015; Drory et al. 2015) and other surveys of  $z \lesssim 0.1$  galaxies. In Figure 12 we make a direct comparison of our MSA-3D case study target with an example galaxy from MaNGA (MaNGA ID 12-129618, plate-

IFU 7495-12704) at  $z = 0.029$ . This MaNGA target is chosen for comparison on the basis of similar spiral morphology and stellar mass ( $M_* = 10^{10.3} M_\odot$ ). Figure 12 shows the color image, H $\alpha$  emission map, H $\alpha$ -based gas velocity field, Balmer decrement (i.e., H $\alpha$ /H $\beta$  flux ratio), and radial metallicity gradient for both the  $z \sim 1$  and  $z \sim 0$  galaxies. We note that the Balmer decrement and metallicity gradient are measured from deprojected radial bins using the same methods as described in Section 3 (while the H $\alpha$  flux and velocity maps are taken directly from the MaNGA DAP output; Westfall et al. 2019). A key difference which is not shown is that the MaNGA target contains an AGN, with LINER emission identified via the BPT diagram at  $R \lesssim 3$  kpc. Our target  $z \sim 1$  galaxy has no detected AGN emission despite sensitive limits (e.g.,  $\lesssim 0.8\%$  of observed H $\alpha$  flux; Figures 6, 7) as described in Section 3.2. An AGN contribution at the level seen in the MaNGA target would be readily detected in our MSA-3D data. Other than nuclear activity, both galaxies show similar structure: spiral morphology, rotating disk kinematics, higher dust attenuation toward the central regions, and gas metallicity decreasing with radius. The data quality is able to reveal subtle quantitative differences in properties such as the radial profiles of the Balmer decrement and metallicity. This comparison demonstrates the ability to make meaningful and detailed comparisons of our  $z \sim 1$  sample with the  $z \sim 0$  galaxy population. JWST/NIRSpec slit-stepping data are thus powerful for galaxy evolution studies.

We emphasize that the MSA-3D slit-stepping data enable excellent spatially resolved measurements for *individual galaxies*, such as the one studied here. This represents a significant advance over previous methods, such as the stacking technique utilized with Hubble Space Telescope grisms, which combined high-resolution optical imaging with low-resolution GRISM spectroscopy to measure radial Balmer decrement and star formation profiles (Nelson et al. 2016a,b). Previous state-of-the-art IFS studies at  $z > 1$  relied on  $\gtrsim 10$  hour integrations with ground-based telescopes and adaptive optics (e.g., Tacchella et al. 2018; Genzel et al. 2020). These deep AO studies typically focus on H $\alpha$  emission (and the nearby [N II] and [S II]), whereas our MSA-3D data cover additional key lines such as [O III] and H $\beta$ , or [S III] and other features depending on the redshift and slit mask placement (Table 1). The wavelength coverage of our MSA-3D observations is largely inaccessible to current AO systems, yet it is invaluable for accurately establishing the spatially resolved dust attenuation, AGN contributions, metallicity, and other properties. Indeed, to our knowledge the results shown in this paper represent the

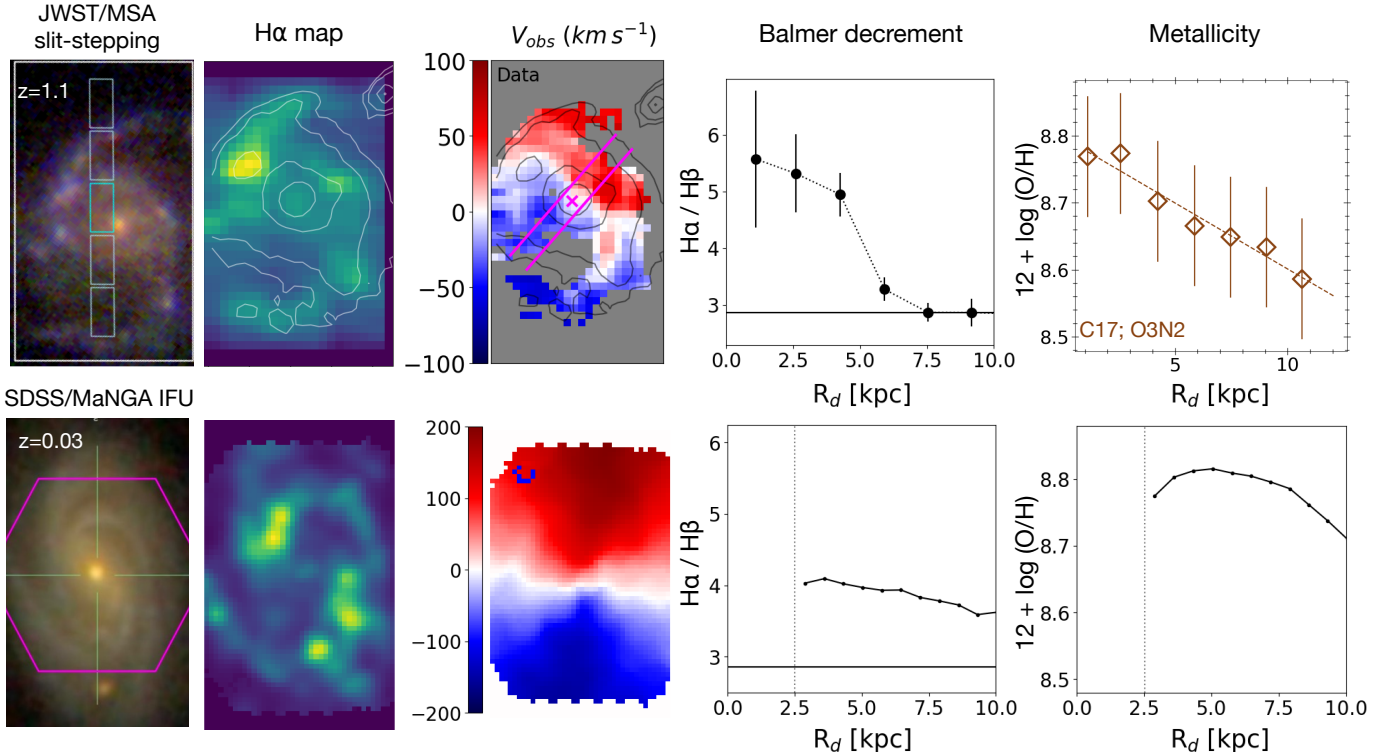


**Figure 12:** Summary of physical measurements for the  $z = 1.104$  galaxy presented in this work (*top*), compared to similar measurements for a galaxy at  $z = 0.029$  obtained from the SDSS MaNGA survey (*bottom*). The galaxies are matched in stellar mass with both having  $M_* = 10^{10.3} M_\odot$ . Both exhibit prominent spiral structure although the  $z \sim 0$  galaxy is more highly inclined on the sky. From left to right, each row shows: the color rest-frame optical image,  $H\alpha$  flux map,  $H\alpha$ -based velocity field, dust attenuation gradient from the Balmer decrement, and metallicity gradient measured from the O3N2 index. The  $z \sim 0$  galaxy contains a clear AGN based on BPT diagnostics which contaminates the inner 2–3 kpc; the central regions are not shown in the attenuation and metallicity gradient plots but may influence values at  $R_d \lesssim 3$  kpc. The  $z \sim 1$  galaxy in contrast has no sign of nuclear supermassive black hole activity. This comparison demonstrates that slit-stepping with the JWST/NIRSpec MSA is capable of efficiently delivering emission line data quality for  $z > 1$  galaxies which is comparable to that available for large samples from MaNGA and other surveys at  $z \sim 0$ . The MSA slit-stepping technique thus offers a promising avenue for comprehensive 3-D spectroscopic studies of galaxy formation across cosmic time.

most robust resolved Balmer decrement, dust-corrected  $H\alpha$  (i.e., SFR), and metallicity maps ever obtained for a  $z \gtrsim 1$  galaxy.

An important conclusion from initial analyses of our MSA-3D program is that the slit-stepping strategy with NIRSpec’s MSA is a *highly effective and efficient method* to observe large samples of galaxies across cosmic time.

As discussed in Section 2.3, slit-stepping is the most cost-effective approach for IFS surveys of populations with projected number density  $\gtrsim 1$  arcmin $^{-2}$ , which can take advantage of NIRSpec/MSA’s multiplexing capability and sensitivity. Slit-stepping is complementary to NIRSpec’s IFU mode, which provides finer spatial sampling and is powerful for studying objects which are rare on the sky. This includes gravitational lenses (e.g., Rigby et al. 2023) and extremely luminous systems (e.g.,

Marshall et al. 2023). Four programs have adopted slit-stepping strategies to date. Our  $\sim 30$  hour JWST Cycle 1 program has already delivered standalone data for 43 galaxies at  $z \sim 1$  with exquisite sensitivity, wavelength coverage, and spatial and spectral resolution. A followup Cycle 2 program (JWST-GO-3426) by our team recently obtained comparable slit-stepping IFS data for 42 galaxies at  $z \simeq 3$  within a single pointing. Two programs from another team have obtained slit-stepping observations of 56 galaxies at  $z = 1$ –5 (JWST-GO-2123), and  $\sim 250$  galaxies at  $z \simeq 3$  (JWST-GO-4291), using a different and complementary dithering strategy. Collectively these four programs represent an investment of just over 200 hours of JWST time allocation – less than the GA-NIFS program which is observing  $\sim 50$  galaxies with the IFU mode.

Given the remarkable efficiency of MSA slit-stepping and its demonstrated success via our MSA-3D program, we advocate for future programs to comprehensively survey the galaxy population across cosmic time using this method. The four programs carried out to date are an excellent start, yet represent a modest subset of cosmic times and galaxy properties (e.g., mass and star formation rate). An IFS sample size equivalent to the KMOS<sup>3D</sup> survey (739 galaxies at  $z = 0.6\text{--}2.7$ ; Wisnioski et al. 2019) would require approximately 600 hours at the depth of our MSA-3D program, which delivers broader wavelength coverage and  $\sim 5\text{--}10$  times better angular resolution than KMOS<sup>3D</sup>. Such a sample can be obtained in  $\lesssim 200$  hours at the shallower depth adopted by the JWST-GO-4291 program. A sample of this size is out of reach for JWST’s IFU modes in its limited mission lifetime, yet it is achievable with MSA slit-stepping. Despite the clear advantages, however, slit-stepping is not an officially supported observing mode and the standard data reduction pipelines are not equipped to handle it. We are mitigating this by publicly releasing our custom pipeline (Section 2.4) and example data products. While we are already addressing the main challenges associated with data processing, we also advocate for further investment in software infrastructure to optimize the scientific return of slit-stepping surveys.

#### ACKNOWLEDGEMENTS

We thank B. Rauscher for developing the NSClean algorithm and making it available. We thank Keerthi G.

C. Vasan for their valuable input. This work is based on observations made with the NASA/ESA/CSA James Webb Space Telescope. The data were obtained from the Mikulski Archive for Space Telescopes at the Space Telescope Science Institute, which is operated by the Association of Universities for Research in Astronomy, Inc., under NASA contract NAS 5-03127 for JWST. These observations are associated with program JWST-GO-2136. We acknowledge financial support from NASA through grant JWST-GO-2136. This work made use of observations and catalogs from the 3D-HST Treasury Program (GO 12177 and 12328) with the NASA/ESA Hubble Space Telescope, which is operated by the Association of Universities for Research in Astronomy, Inc., under NASA contract NAS5-26555. XW and MJ are supported by the National Natural Science Foundation of China (grant 12373009), the CAS Project for Young Scientists in Basic Research Grant No. YSBR-062, the Fundamental Research Funds for the Central Universities, the Xiaomi Young Talents Program, and the science research grant from the China Manned Space Project. CAFG was supported by NSF through grants AST-2108230 and AST-2307327; by NASA through grant 21-ATP21-0036; and by STScI through grant JWST-AR-03252.001-A. J.M.E.S. acknowledges financial support from the European Research Council (ERC) Advanced Grant under the European Union’s Horizon Europe research and innovation programme (grant agreement AdG GALPHYS, No. 101055023).

*Facilities:* JWST (NIRSpec MSA)

#### REFERENCES

- Abazajian, K. N., Adelman-McCarthy, J. K., Agüeros, M. A., et al. 2009, *ApJS*, 182, 543
- Baker, J. G., & Menzel, D. H. 1938, *ApJ*, 88, 52
- Baldwin, J. A., Phillips, M. M., & Terlevich, R. 1981, *PASP*, 93, 5
- Belfiore, F., Maiolino, R., Tremonti, C., et al. 2017, *MNRAS*, 469, 151
- Bell, E. F., & de Jong, R. S. 2001, *ApJ*, 550, 212
- Belli, S., Genzel, R., Förster Schreiber, N. M., et al. 2017, *ApJL*, 841, L6
- Bennett, C. L., Larson, D., Weiland, J. L., & Hinshaw, G. 2014, *ApJ*, 794, 135
- Bland-Hawthorn, J., & Gerhard, O. 2016, *ARA&A*, 54, 529
- Böker, T., Beck, T. L., Birkmann, S. M., et al. 2023, *PASP*, 135, 038001
- Bouché, N., Carfantan, H., Schroetter, I., Michel-Dansac, L., & Contini, T. 2015, *AJ*, 150, 92
- Bourne, N., Dunlop, J. S., Merlin, E., et al. 2017, *MNRAS*, 467, 1360
- Bouwens, R. J., Aravena, M., Decarli, R., et al. 2016, *ApJ*, 833, 72
- Brammer, G. B., van Dokkum, P. G., Franx, M., et al. 2012, *ApJS*, 200, 13
- Brennan, R., Pandya, V., Somerville, R. S., et al. 2017, *MNRAS*, 465, 619
- Bundy, K., Bershady, M. A., Law, D. R., et al. 2015, *ApJ*, 798, 7
- Burkert, A., Förster Schreiber, N. M., Genzel, R., et al. 2016, *ApJ*, 826, 214
- Buta, R., & Combes, F. 1996, *FCPh*, 17, 95
- Byrne, L., Faucher-Giguère, C.-A., Stern, J., et al. 2023, *MNRAS*, 520, 722
- Calzetti, D., Armus, L., Bohlin, R. C., et al. 2000, *ApJ*, 533, 682

- Charlot, S., & Fall, S. M. 2000, *ApJ*, 539, 718
- Courteau, S. 1997, *AJ*, 114, 2402
- Curti, M., Cresci, G., Mannucci, F., et al. 2017, *MNRAS*, 465, 1384
- Curti, M., Maiolino, R., Cirasuolo, M., et al. 2020, *MNRAS*, 492, 821
- Davies, R., Förster Schreiber, N. M., Cresci, G., et al. 2011, *ApJ*, 741, 69
- Dekel, A., Sari, R., & Ceverino, D. 2009, *ApJ*, 703, 785
- Domínguez, A., Siana, B., Henry, A. L., et al. 2013, *ApJ*, 763, 145
- Drory, N., MacDonald, N., Bershady, M. A., et al. 2015, *AJ*, 149, 77
- Elmegreen, B. G., & Elmegreen, D. M. 2006, *ApJ*, 650, 644
- Epinat, B., Amram, P., Marcelin, M., et al. 2008, *MNRAS*, 388, 500
- Epinat, B., Contini, T., Le Fèvre, O., et al. 2009, *A&A*, 504, 789
- Epinat, B., Tasca, L., Amram, P., et al. 2012, *A&A*, 539, A92
- Espejo Salcedo, J. M., Glazebrook, K., Fisher, D. B., et al. 2022, *MNRAS*, 509, 2318
- Faucher-Giguère, C.-A., & Oh, S. P. 2023, *ARA&A*, 61, 131
- Faucher-Giguère, C.-A., Quataert, E., & Hopkins, P. F. 2013, *MNRAS*, 433, 1970
- Ferruit, P., Jakobsen, P., Giardino, G., et al. 2022, *A&A*, 661, A81
- Finkelstein, S. L., Bagley, M. B., Ferguson, H. C., et al. 2023, *ApJL*, 946, L13
- Forbes, J. C., Emami, R., Somerville, R. S., et al. 2023, *ApJ*, 948, 107
- Foreman-Mackey, D., Hogg, D. W., Lang, D., & Goodman, J. 2013, *PASP*, 125, 306
- Förster Schreiber, N. M., & Wuyts, S. 2020, *ARA&A*, 58, 661
- Förster Schreiber, N. M., Genzel, R., Bouché, N., et al. 2009, *ApJ*, 706, 1364
- Förster Schreiber, N. M., Shapley, A. E., Genzel, R., et al. 2011, *ApJ*, 739, 45
- Förster Schreiber, N. M., Renzini, A., Mancini, C., et al. 2018, *ApJS*, 238, 21
- Freeman, K. C. 1970, *ApJ*, 160, 811
- Genzel, R., Tacconi, L. J., Eisenhauer, F., et al. 2006, *Nature*, 442, 786
- Genzel, R., Burkert, A., Bouché, N., et al. 2008, *ApJ*, 687, 59
- Genzel, R., Tacconi, L. J., Kurk, J., et al. 2013, *ApJ*, 773, 68
- Genzel, R., Price, S. H., Übler, H., et al. 2020, *ApJ*, 902, 98
- Gibson, B. K., Pilkington, K., Brook, C. B., Stinson, G. S., & Bailin, J. 2013, *A&A*, 554, A47
- Glazebrook, K. 2013, *PASA*, 30, e056
- Green, J. D., & Olszewski, H. 2020, *IR Snowball Occurrences in WFC3/IR: 2009-2019, Instrument Science Report WFC3 2020-3, ,*
- Guo, Y., Ferguson, H. C., Bell, E. F., et al. 2015, *ApJ*, 800, 39
- Gurvich, A. B., Stern, J., Faucher-Giguère, C.-A., et al. 2023, *MNRAS*, 519, 2598
- Hafen, Z., Stern, J., Bullock, J., et al. 2022, *MNRAS*, 514, 5056
- Hamilton-Campos, K. A., Simons, R. C., Peeples, M. S., Snyder, G. F., & Heckman, T. M. 2023, *arXiv e-prints*, arXiv:2303.04171
- Heinis, S., Buat, V., Béthermin, M., et al. 2014, *MNRAS*, 437, 1268
- Hemler, Z. S., Torrey, P., Qi, J., et al. 2021, *MNRAS*, 506, 3024
- Hirtenstein, J., Jones, T., Wang, X., et al. 2019, *ApJ*, 880, 54
- Ho, I. T., Seibert, M., Meidt, S. E., et al. 2017, *ApJ*, 846, 39
- Hopkins, P. F., Gurvich, A. B., Shen, X., et al. 2023, *MNRAS*, arXiv:2301.08263
- Hubble, E. P. 1926, *ApJ*, 64, 321
- Jakobsen, P., Ferruit, P., Alves de Oliveira, C., et al. 2022, *A&A*, 661, A80
- Jones, G. C., Vergani, D., Romano, M., et al. 2021, *MNRAS*, 507, 3540
- Jones, T., Ellis, R. S., Richard, J., & Jullo, E. 2013, *ApJ*, 765, 48
- Jones, T., Martin, C., & Cooper, M. C. 2015a, *ApJ*, 813, 126
- Jones, T., Wang, X., Schmidt, K. B., et al. 2015b, *AJ*, 149, 107
- Jones, T. A., Swinbank, A. M., Ellis, R. S., Richard, J., & Stark, D. P. 2010, *MNRAS*, 404, 1247
- Ju, M., Yin, J., Liu, R., et al. 2022, *ApJ*, 938, 96
- Kashino, D., Silverman, J. D., Rodighiero, G., et al. 2013, *ApJL*, 777, L8
- Kassin, S. A., Weiner, B. J., Faber, S. M., et al. 2012, *ApJ*, 758, 106
- Kennicutt, Robert C., J. 1998, *ARA&A*, 36, 189
- Kewley, L. J., Dopita, M. A., Leitherer, C., et al. 2013, *ApJ*, 774, 100
- Kewley, L. J., Nicholls, D. C., & Sutherland, R. S. 2019, *ARA&A*, 57, 511
- Kewley, L. J., Rupke, D., Zahid, H. J., Geller, M. J., & Barton, E. J. 2010, *ApJL*, 721, L48

- Koekemoer, A. M., Faber, S. M., Ferguson, H. C., et al. 2011, *ApJS*, 197, 36
- Kriek, M., Shapley, A. E., Reddy, N. A., et al. 2015, *ApJS*, 218, 15
- Kuhn, V., Guo, Y., Martin, A., et al. 2024, *ApJL*, 968, L15
- Leethochawalit, N., Jones, T. A., Ellis, R. S., et al. 2016, *ApJ*, 820, 84
- Lian, J., Zasowski, G., Chen, B., et al. 2024, arXiv e-prints, arXiv:2406.05604
- Lin, L., Hsieh, B.-C., Pan, H.-A., et al. 2019, *ApJ*, 872, 50
- Livermore, R. C., Jones, T. A., Richard, J., et al. 2015, *MNRAS*, 450, 1812
- Lorenz, B., Kriek, M., Shapley, A. E., et al. 2023, *ApJ*, 951, 29
- Ly, C., Malkan, M. A., Kashikawa, N., et al. 2012, *ApJL*, 747, L16
- Ma, X., Hopkins, P. F., Feldmann, R., et al. 2017, *MNRAS*, 466, 4780
- Maiolino, R., & Mannucci, F. 2019, *A&A Rv*, 27, 3
- Margalef-Bentabol, B., Conselice, C. J., Haeussler, B., et al. 2022, *MNRAS*, 511, 1502
- Marshall, M. A., Perna, M., Willott, C. J., et al. 2023, *A&A*, 678, A191
- McGaugh, S. S., & Schombert, J. M. 2014, *AJ*, 148, 77
- McLure, R. J., Dunlop, J. S., Cullen, F., et al. 2018, *MNRAS*, 476, 3991
- Miller, S. H., Bundy, K., Sullivan, M., Ellis, R. S., & Treu, T. 2011, *ApJ*, 741, 115
- Miller, S. H., Ellis, R. S., Sullivan, M., et al. 2012, *ApJ*, 753, 74
- Momcheva, I. G., Brammer, G. B., van Dokkum, P. G., et al. 2016, *ApJS*, 225, 27
- Mortlock, A., Conselice, C. J., Hartley, W. G., et al. 2013, *MNRAS*, 433, 1185
- Nanayakkara, T., Glazebrook, K., Jacobs, C., et al. 2023, *ApJL*, 947, L26
- Nelson, E. J., van Dokkum, P. G., Förster Schreiber, N. M., et al. 2016a, *ApJ*, 828, 27
- Nelson, E. J., van Dokkum, P. G., Momcheva, I. G., et al. 2016b, *ApJL*, 817, L9
- Newman, J. A., Cooper, M. C., Davis, M., et al. 2013, *ApJS*, 208, 5
- Osterbrock, D. E., & Ferland, G. J. 2006, *Astrophysics of gaseous nebulae and active galactic nuclei*
- Perna, M. 2023, in *IAU Symposium, Vol. 373, Resolving the Rise and Fall of Star Formation in Galaxies*, ed. T. Wong & W.-T. Kim, 60–62
- Pettini, M., & Pagel, B. E. J. 2004, *MNRAS*, 348, L59
- Pillepich, A., Nelson, D., Springel, V., et al. 2019, *MNRAS*, 490, 3196
- Price, S. H., Kriek, M., Brammer, G. B., et al. 2014, *ApJ*, 788, 86
- Rauscher, B. J. 2023, arXiv e-prints, arXiv:2306.03250
- Rich, J. A., Torrey, P., Kewley, L. J., Dopita, M. A., & Rupke, D. S. N. 2012, *ApJ*, 753, 5
- Rigby, J. R., Vieira, J. D., Phadke, K. A., et al. 2023, arXiv e-prints, arXiv:2312.10465
- Sánchez Almeida, J., Elmegreen, B. G., Muñoz-Tuñón, C., et al. 2015, *ApJL*, 810, L15
- Sanders, R. L., Shapley, A. E., Reddy, N. A., et al. 2020, *MNRAS*, 491, 1427
- Shapley, A. E., Sanders, R. L., Salim, S., et al. 2022, *ApJ*, 926, 145
- Simons, R. C., Kassin, S. A., Trump, J. R., et al. 2016, *ApJ*, 830, 14
- Simons, R. C., Kassin, S. A., Weiner, B. J., et al. 2017, *ApJ*, 843, 46
- Simons, R. C., Kassin, S. A., Snyder, G. F., et al. 2019, *ApJ*, 874, 59
- Simons, R. C., Papovich, C., Momcheva, I., et al. 2021, *ApJ*, 923, 203
- Skelton, R. E., Whitaker, K. E., Momcheva, I. G., et al. 2014, *ApJS*, 214, 24
- Speagle, J. S., Steinhardt, C. L., Capak, P. L., & Silverman, J. D. 2014, *ApJS*, 214, 15
- Stark, D. P., Swinbank, A. M., Ellis, R. S., et al. 2008, *Nature*, 455, 775
- Stern, J., Faucher-Giguère, C.-A., Fielding, D., et al. 2021, *ApJ*, 911, 88
- Storey, P. J., & Hummer, D. G. 1995, *MNRAS*, 272, 41
- Stott, J. P., Swinbank, A. M., Johnson, H. L., et al. 2016, *MNRAS*, 457, 1888
- Straatman, C. M. S., Spitler, L. R., Quadri, R. F., et al. 2016, *ApJ*, 830, 51
- Swinbank, A. M., Papadopoulos, P. P., Cox, P., et al. 2011, *ApJ*, 742, 11
- Tacchella, S., Carollo, C. M., Förster Schreiber, N. M., et al. 2018, *ApJ*, 859, 56
- Tacconi, L. J., Neri, R., Genzel, R., et al. 2013, *ApJ*, 768, 74
- Tiley, A. L., Gillman, S., Cortese, L., et al. 2021, *MNRAS*, 506, 323
- Tumlinson, J., Peebles, M. S., & Werk, J. K. 2017, *ARA&A*, 55, 389
- Turner, O. J., Cirasuolo, M., Harrison, C. M., et al. 2017, *MNRAS*, 471, 1280
- Übler, H., Genzel, R., Wisnioski, E., et al. 2019, *ApJ*, 880, 48
- van der Wel, A., Franx, M., van Dokkum, P. G., et al. 2014, *ApJ*, 788, 28
- van Dokkum, P. G. 2001, *PASP*, 113, 1420

- van Dokkum, P. G., Kriek, M., Rodgers, B., Franx, M., & Puxley, P. 2005, *ApJL*, 622, L13
- Wang, X., Jones, T. A., Treu, T., et al. 2017, *ApJ*, 837, 89
- Wang, X., Jones, T. A., Treu, T., et al. 2019, *The Astrophysical Journal*, 882, 94
- Wang, X., Jones, T. A., Treu, T., et al. 2020, *ApJ*, 900, 183
- Wang, X., Jones, T., Vulcani, B., et al. 2022, *ApJL*, 938, L16
- Westfall, K. B., Cappellari, M., Bershady, M. A., et al. 2019, *AJ*, 158, 231
- Whitaker, K. E., Pope, A., Cybulski, R., et al. 2017, *ApJ*, 850, 208
- Whitaker, K. E., van Dokkum, P. G., Brammer, G., & Franx, M. 2012, *ApJL*, 754, L29
- Whitaker, K. E., Franx, M., Leja, J., et al. 2014, *ApJ*, 795, 104
- Wisnioski, E., Förster Schreiber, N. M., Wuyts, S., et al. 2015, *ApJ*, 799, 209
- Wisnioski, E., Förster Schreiber, N. M., Fossati, M., et al. 2019, *ApJ*, 886, 124
- Wright, S. A., Larkin, J. E., Graham, J. R., & Ma, C.-P. 2010, *ApJ*, 711, 1291
- Wu, Y., Cai, Z., Sun, F., et al. 2023, *ApJL*, 942, L1
- Wuyts, S., Förster Schreiber, N. M., van der Wel, A., et al. 2011, *ApJ*, 742, 96
- Wuyts, S., Förster Schreiber, N. M., Nelson, E. J., et al. 2013, *ApJ*, 779, 135
- Yuan, T. T., Kewley, L. J., & Rich, J. 2013, *ApJ*, 767, 106
- Zhang, H., Primack, J. R., Faber, S. M., et al. 2019, *MNRAS*, 484, 5170